# The equilibrium of rubble-pile satellites: The Darwin and Roche ellipsoids for gravitationally held granular aggregates

Ishan Sharma

*Department of Mechanical Engineering, IIT Kanpur, Kanpur 208016, India.*

**Abstract**

Many new small moons of the giant planets have been discovered recently. In parallel, satellites of several asteroids, e.g., Ida, have been found. Strikingly, a majority of these new-found planetary moons are estimated to have very low densities, which, along with their hypothesized accretionary origins, suggests a rubble internal structure. This, coupled to the fact that many asteroids are also thought to be particle aggregates held together principally by self-gravity, motivates the present investigation into the possible ellipsoidal shapes that a rubble-pile satellite may achieve as it orbits an *a*spherical primary. Conversely, knowledge of the shape will constrain the granular aggregate's orbit - the closer it gets to a primary, both primary's tidal effect and the satellite's spin are greater. We will assume that the primary body is sufficiently massive so as not to be influenced by the satellite. However, we will incorporate the primary's possible ellipsoidal shape, e.g., flattening at its poles in the case of a planet, and the proloidal shape of asteroids. In this, the present investigation is an extension of the first classical Darwin problem to granular aggregates.

General equations defining an ellipsoidal rubble pile's equilibrium about an ellipsoidal primary are developed. They are then utilized to scrutinize the possible granular nature of small inner moons of the giant planets. It is found that most satellites satisfy constraints necessary to exist as equilibrated granular aggregates. Objects like Naiad, Metis and Adrastea appear to violate these limits, but in doing so, provide clues to their internal density and/or structure. We also recover the Roche limit for a granular satellite of a spherical primary, and employ it to study the Martian satellites, Phobos and Deimos, as well as to make contact with earlier work of Davidsson (*Icarus* **149** [2001], 375). The satellite's interior will be modeled as a rigid-plastic, cohesion-less material with a Drucker-Prager yield criterion. This rheology is a reasonable first model for rubble piles. We will employ an approximate volume-averaging procedure that is based on the classical method of moments, and is an extension of the virial method (S. Chandrasekhar, *Ellipsoidal Figures of Equilibrium*, Yale U. Press [1969]) to granular solid bodies.

## 1 Introduction

Roche (1847) first considered the problem of finding the equilibrium shape of a fluid satellite of a spherical planet, identifying ellipsoidal equilibrium shapes now known as the Roche ellipsoids. Later, Darwin (1906) introduced a non-trivial generalization of the Roche problem: the characterization of equilibrium shapes of two tidally interacting fluid bodies that rotate about each other on circular orbits. Chandrasekhar (1969) showed that, at least in the case of fluids, there are only two possible scenarios in which such ellipsoidal equilibrium shapes may be found. The first is when the *a*spherical primary is massive enough to warrant neglecting the tidal effects due to the satellite. In the other case, both objects are congruent, i.e., with the same shape, mass and in a symmetric orientation. Indeed, Darwin (1906) himself had emphasized this dichotomy. We will refer to this natural classification as the *first* and *second* Darwin problems, whose solution, for an *inviscid fluid*, yields the Darwin sequence of ellipsoids (Chandrasekhar 1969).

Recently, several small inner moons of the giant planets have been discovered. Their estimated low densities, often lower than or comparable to water's, suggests that these objects may be either granular aggregates, or highly porous cellular "honeycomb"-like structures. While the former, in the absence of cohesion, has no tensile strength and is held together only by its own gravity, the latter is able to withstand a certain amount of tension. It is, however, believed that these newly uncovered satellites may have formed via an accretionary process either from ring particles, as in the case of Saturn's moons (Porco et al. 2007), or from the debris left over from some past catastrophic event, e.g., Neptune's capture of Triton (Banfield and Murray 1992). There is thus a need to generalize the first of the two classical Darwin problems introduced above to *rubble-pile* satellites of *oblate* planets. In fact, the finding of asteroidal satellites, many of which are suspected particle aggregates, strongly suggests the need to consider also elongated triaxial primaries. The general scenario is displayed in Fig. 1.

Rubble piles, while much weaker than coherent structures, are able to sustain shear stresses due to internal friction. This allows a range of stable satellite shapes to be possible at a given planetary distance. Conversely, for a given shape, the satellite's orbits on which it may persist in equilibrium are not necessarily unique. In the sequel, we will obtain general equations that describe the equilibrium landscape of a triaxial-ellipsoidal, tidally-locked, rubble-pile satellite on a circular orbit around a triaxial-ellipsoidal primary. The formulation will then be specialized to investigate the moons of the giant planets. In Sec. 5, the Roche limit for a granular aggregate, i.e., the critical distance at

*Email address:* ishans@iitk.ac.in (Ishan Sharma).

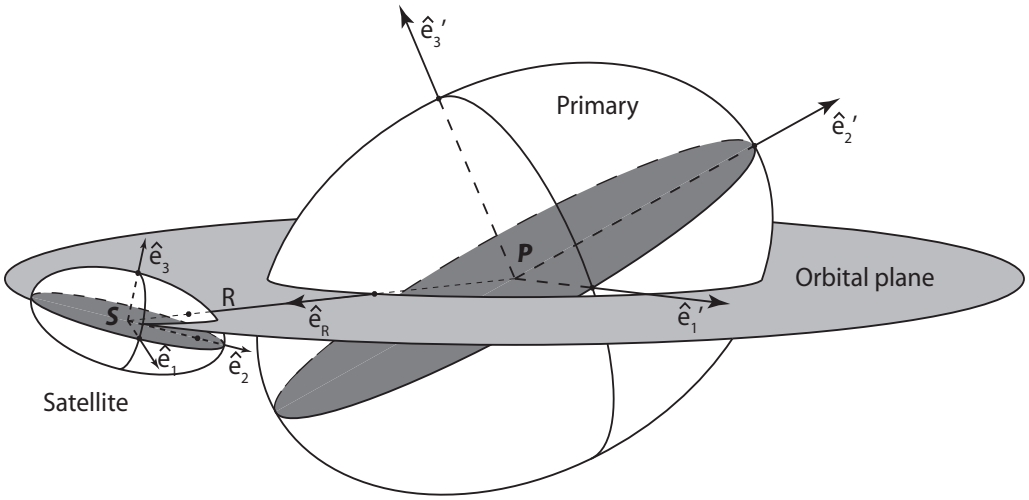


Fig. 1. The general configuration of an ellipsoidal satellite of an ellipsoidal primary. The unit vector $\hat{\mathbf{e}}_R$ locates the satellite with respect to the primary's center.

which a rubble-pile satellite may orbit a spherical planet, will also be obtained as a special case and will then be employed to study the two satellites of Mars. Recently, Holsapple and Michel (2006, 2008) have considered the Roche limit for solid bodies, employing the static version of Signorini's theory of stress means (Truesdell and Toupin 1960, p. 574). We compare briefly with their results in Sec. 5.2.

We will employ a volume-averaging procedure that is really a generalization of Chandrasekhar's (1969) virial method to the statics, and dynamics, of solid objects. Previously, this volume-averaging procedure has been employed to investigate tidal disruption during planetary flybys (Sharma 2004, Sharma et al. 2006), equilibrium shapes and dynamical passage into them for asteroids in pure spin (Sharma et al. 2005a, 2005b, 2008), and the Roche limit for rubble piles (Sharma et al. 2005b, Burns et al. 2007). A good match with available computational and analytical results was achieved. In fact, in the case of rubble piles in pure spin, the equilibrium landscape obtained from volume-averaging matched perfectly Holsapple's (2001) exact results that were based on rigorous limit analysis (Chen and Han 1988) often employed in rigid-plasticity.

We develop the governing equations next.

## 2 Volume-averaging

In this section, we present the main equations obtained from an application of the volume-averaging procedure. More details about derivations may be found in Chandrasekhar (1969), Sharma et al. (2006), or Sharma et al. (2008).

In case of a tidally interacting satellite, there are principal-axes coordinate systems associated with both the satellite and the primary. No particular system is better suited to evaluate all quantities that will appear below. In addition, many different relative orientations of the primary and the satellite are possible. Thus, it is advantageous to follow a coordinate-independent tensor-based approach. We will develop general equations, applicable to all primary-satellite configurations, as far as possible, and only specialize to a particular primary-satellite configuration at the very end. We offer a very short primer on tensors and operations with them in Appendix A. More information may be obtained from Knowles (1998). The reader should also refer to Appendix A for notations followed in this paper.

We now proceed to the governing equations.

### *2.1 Governing equations*

We consider a finite-sized satellite in motion about a primary also of finite spatial extent. Much work has been done on the dynamical problem of relative equilibria in the two finite rigid-body problem, and we refer the interested reader to Kinoshita (1972), and more recently to Scheeres (2006). Indeed, the two finite rigid-body problem will be relevant when extending the present work to the equilibrium shapes in a binary system consisting of comparable masses, i.e., the second Darwin problem introduced in Sec. 1. In this paper, we focus on the first Darwin problem, wherein the primary is much more massive than the satellite. Thus, we neglect the motion of the primary's center of mass. We also make the further assumption that the satellite moves around the primary at a much faster rate than the primary around the Sun.

The stress $\boldsymbol{\sigma}$ inside a deformable body, such as a satellite, may be obtained by solving the Navier equation (see, e.g., Fung 1965)

$$\boldsymbol{\nabla} \cdot \boldsymbol{\sigma} + \rho \mathsf{b} = \rho \left( \ddot{\mathsf{x}} + \ddot{\mathsf{R}} \right), \tag{1}$$

where $\rho$ is the density, $\mathsf{b}$ the body force and $\mathsf{x}$ the location of a material point with respect to the satellite's center of mass, and $\mathsf{R}$ locates the satellite's moving mass center with respect to the primary's fixed center of mass (see Fig. 1). To solve the above partial differential equation, one must provide appropriate boundary conditions, and compatibility equations that incorporate the material's constitutive behavior. Note that, within the approximations introduced in the preceding paragraph, $\ddot{\mathsf{x}} + \ddot{\mathsf{R}}$ is the total acceleration of a material point and $\ddot{\mathsf{x}}$ is the acceleration relative to the satellite's mass center. The body force includes in our case the tidal effects of the primary on the satellite, and of the satellite's internal gravity on itself. Except in the simplest of geometries, loading conditions, rheologies and small deformations, solving for the exact

stresses is often analytically intractable, and even computationally very involved. Considering the intricate constitutive nature of planetary bodies, the utility of undertaking such an exercise is also moot. Instead we follow an approximate method here.

Volume-averaging begins by making systematic approximations to the body's actual time-varying deformation field in terms of a finite number of only temporally dependent variables. Equations governing these variables are then obtained by taking an appropriate order moment of the linear momentum balance equation (1) above. For example, the first moment, and the one utilized in this work, is obtained by integrating the tensor product (A.2) of each quantity in (1) with the position vector $\mathsf{x}$ over the body's volume $V$. This has the advantage of converting the governing coupled non-linear partial differential equations into a set of ordinary differential equations, easily integrated by a Runge-Kutta time-marching algorithm. The disadvantage is that our solutions are valid on a global, rather than local, scale. The volume-averaging procedure is reminiscent of the Galerkin projection frequently employed in finite element analysis (e.g., Belytschko et al. 2000), and, in fact, an exact equivalence may be demonstrated.

Here we consider the simplest non-trivial such kinematic assumption suitable to the problem at hand; a deformation that is homogeneous when viewed in a *non-rotating* coordinate system with its origin at the ellipsoidal satellite's mass center. We assume that the ellipsoidal satellite is homogeneous, so that its mass and geometric centers coincide. Physically, this kinematic assumption enforces the condition that, in this coordinate system that orbits the primary along with the satellite, but does not rotate with the latter, an initially ellipsoidal shape deforms only into another ellipsoid. As noted earlier (Sharma et al. 2008), homogeneous kinematics were shown to yield physically meaningful results in the case of spinning fluid masses by Chandrasekhar (1969). Further motivation is provided by the fact that spinning elastic ellipsoids, and also tidally-stressed elastic ellipsoids, deform into ellipsoids (Love 1946, Murray and Dermott 1999).

With the above kinematic assumption, the original position $\mathsf{x}_0$ of a mass point with respect to the satellite's center of mass may now be related to its future location $\mathsf{x}$ by

$$\mathsf{x} = \boldsymbol{F} \cdot \mathsf{x}_0, \tag{2}$$

in terms of the *deformation gradient tensor* $\boldsymbol{F}$ that depends only on time, and *not* on the spatial coordinates. Thus, $\boldsymbol{F}$ incorporates the nine independent temporal variables that we assume approximate the ellipsoid's actual deformation. These variables roughly correspond to three stretches, three shears and three rotations. For a rigid body, $\boldsymbol{F}$ is a rotation tensor. Rather than developing equations for the components of $\boldsymbol{F}$, as Sharma et al. (2006, 2008)

did, we first introduce the *velocity gradient*

$$\boldsymbol{L} = \dot{\boldsymbol{F}} \cdot \boldsymbol{F}^{-1}, \tag{3}$$

so that the kinematic law (2) may be replaced by its equivalent incremental form

$$\dot{\mathsf{x}} = \boldsymbol{L} \cdot \mathsf{x}. \tag{4}$$

Like $\boldsymbol{F}$, $\boldsymbol{L}$ is also independent of $\mathsf{x}$, depending only on time.

As indicated above, a sufficient number of equations for the components of $\boldsymbol{L}$ are obtained by taking the first moment of (1), invoking the divergence theorem to transform volume integrals, employing (3) to represent the velocities $\dot{\mathsf{x}}$ and accelerations $\ddot{\mathsf{x}}$ in terms of the position vector $\mathsf{x}$ and $\boldsymbol{L}$, and finally assuming a traction-free (force-free) surface. The resulting volume-averaged evolution equation for $\boldsymbol{L}$ is

$$\left(\dot{\boldsymbol{L}} + \boldsymbol{L}^2\right) \cdot \boldsymbol{I} = \boldsymbol{M}^T - \overline{\boldsymbol{\sigma}} V, \tag{5}$$

where $\overline{\boldsymbol{\sigma}}$ is now the average stress $(1/V) \int_V \sigma dV$,

$$\boldsymbol{I} = \int_V \rho \mathsf{x} \otimes \mathsf{x} dV \tag{6}$$

is the inertia tensor, and

$$\boldsymbol{M} = \int_V \mathsf{x} \otimes \rho \mathsf{b} dV \tag{7}$$

is the moment tensor due to the body forces $\mathsf{b}$. In the development above, the term $\int_V \mathsf{x} \otimes \ddot{\mathsf{R}} \rho dV = \int_V \mathsf{x} \rho dV \otimes \ddot{\mathsf{R}}$ vanished because the satellite's center of mass is at $\mathsf{x} = 0$. We note that under the assumption of homogeneous kinematics, the deformation and velocity gradients are constant throughout the body. Therefore the stresses too are independent of $\mathsf{x}$, as they typically depend only on $\boldsymbol{F}$ and $\boldsymbol{L}$. Consequently, the average stress $\overline{\boldsymbol{\sigma}}$ equals the actual stress $\boldsymbol{\sigma}$, and we subsequently drop the overbar on $\overline{\boldsymbol{\sigma}}$.

The inertia tensor's evolution may be followed by first differentiating (6) while conserving mass, and then invoking (4) and (6) to obtain

$$\dot{\boldsymbol{I}} = \boldsymbol{L} \cdot \boldsymbol{I} + (\boldsymbol{I} \cdot \boldsymbol{L})^T. \tag{8}$$

Equations (3), (5) and (8) govern the motion of a homogeneously deforming ellipsoid under the action of only the body forces $\mathsf{b}$, once a constitutive law relating the stress $\boldsymbol{\sigma}$ to the body's deformation is specified.

In general, the velocity gradient incorporates both the strain (or *stretching*) rate and the *spin* rate. The latter rate measures the *local* angular velocity in a deformable medium, and is usually distinct from the rotation rate of the body's principal axes. When the object is rigid, the strain rate vanishes and

the local spin rate coincides with the principal axes' rotation rate. Thus in (5) we set $\boldsymbol{L} = \boldsymbol{W}$, the anti-symmetric tensor associated with the rigid body's angular velocity (see (A.9)), to obtain

$$\left(\dot{\boldsymbol{W}} + \boldsymbol{W}^2\right) \cdot \boldsymbol{I} = \boldsymbol{M}^T - \boldsymbol{\sigma} V. \tag{9}$$

The three Euler equations (Greenwood 1988) governing a rigid body's dynamics are recovered from the nine equations of (9) by taking its anti-symmetric part, and noting that $\boldsymbol{\sigma}$ is symmetric. The remaining six equations yield the *exact* average stress inside the rigid body. Note that while it is impossible to define a point-wise stress field in a *rigid* body, an average stress is well-defined and exactly obtainable, as is done above.

In the present analysis, we are concerned with *tidally-locked equilibrium* configurations of an ellipsoidal satellite on a *circular orbit*. Thus, the spin tensor $\boldsymbol{W}$ associated with the satellite's rotation rate equals the satellite's fixed orbital angular velocity. A constant $\boldsymbol{W}$ is achieved when the torque given by the anti-symmetric part of $\boldsymbol{M}$ vanishes, and the object spins about an axis of principal inertia. Under these conditions, $\boldsymbol{W}$ and $\boldsymbol{I}$ commute and $\boldsymbol{W}^2 \cdot \boldsymbol{I}$ is symmetric. Setting $\dot{\boldsymbol{W}}$ to zero in (9), and rewriting slightly, we find

$$\boldsymbol{\sigma} = \frac{1}{V}\left(\boldsymbol{M}^T - \boldsymbol{W}^2 \cdot \boldsymbol{I}\right), \tag{10}$$

which is a volume-averaged balance between "centrifugal" stresses due to the satellite's rotation, stresses due to the body force as given by the body force moment tensor $\boldsymbol{M}$, and the satellite's internal strength. The above balance, along with a suitable failure law, will help put constraints on a satellite's equilibrium shapes for a given spin and orbit size, as we illustrate below. We emphasize that the above equation is valid for all ellipsoidal satellites and primaries, with the only requirement being that the former be tidally locked and on circular orbit about the latter. To address satellites that are not tidally locked and/or on elliptic orbits, we will have to retain the term $\dot{\boldsymbol{W}}$ in the above equation.

To obtain $\boldsymbol{\sigma}$ from (10), we require both $\boldsymbol{M}$ and $\boldsymbol{W}$. Because we consider tidally-locked satellites, $\boldsymbol{W}$ will be obtained from the satellite's orbital motion in Sec. 2.4. We first calculate the body-force moment tensor $\boldsymbol{M}$. Recall that in our case the body force is due both to the satellite's internal gravity and also the tidal stresses introduced by the primary. Thus, we may write

$$\boldsymbol{M} = \boldsymbol{M}_G + \boldsymbol{M}_Q, \tag{11}$$

where $\boldsymbol{M}_G$ is the moment tensor due to internal gravity, and $\boldsymbol{M}_Q$, the quadrupole moment tensor, is the moment tensor due to tidal influence of the primary. The expressions developed in the following two subsections are applicable to all mutually interacting triaxial-ellipsoidal objects on possibly elliptical orbits.

A cautionary comment is in order here. Consider finding at a point within the satellite the total body force per unit mass due to both the finite-sized satellite and the primary. This body force at this point may be derived, as we do, by adding to the internal gravity force of the satellite, the external gravitational attraction of the primary. It may also be obtained by taking the gradient of the total gravitational potential at that point of each body. The total gravitational potential at a satellite's internal point is the sum of the satellite's internal potential and the primary's external potential. It is important to note that we are *not* attempting to find the mutual potential of two finite-sized objects. This latter potential has been computed by many authors, see, e.g., Werner and Scheeres 2005; Ashenberg 2005, and is of interest when calculating the total energy of the system, which, however, is not the aim here.

### *2.2 Gravitational moment tensor*

$\boldsymbol{M}_G$ was derived in Sharma et al. (2006), and is

$$\boldsymbol{M}_G = -2\pi\rho G \boldsymbol{I}\cdot\boldsymbol{A}, \tag{12}$$

where $G$ is the gravitational constant and the *gravitational shape tensor* $\boldsymbol{A}$ describes the influence of the satellite's ellipsoidal shape on its internal gravity (Chandrasekhar 1969; Sharma et al. 2006). The *symmetric* tensor $\boldsymbol{A}$ depends only on the axes ratios $\alpha = a_2/a_1$ and $\beta = a_3/a_1$, and is completely known for any given ellipsoidal satellite. Moreover, like $\boldsymbol{I}$, it is diagonalized in the satellite's principal-axes coordinate system. Thus, $\boldsymbol{I}$ and $\boldsymbol{A}$ commute. Relevant formulae for the components of $\boldsymbol{A}$ for general ellipsoidal shapes are available (Sharma et al. 2008, Sec. 2.4). We repeat them here for convenience. In its principal-axes coordinate system, for an oblate spheroidal satellite ($1 = \alpha > \beta$), we have

$$A_1 = A_2 = -\frac{\beta^2}{1-\beta^2} + \frac{\beta}{(1-\beta^2)^{3/2}}\sin^{-1}\sqrt{1-\beta^2}, \tag{13}$$

while for prolate objects ($1 > \alpha = \beta$),

$$A_2 = A_3 = \frac{1}{1-\beta^2} - \frac{\beta^2}{2(1-\beta^2)^{3/2}}\ln\left(\frac{1+\sqrt{1-\beta^2}}{1-\sqrt{1-\beta^2}}\right), \tag{14}$$

and finally for truly triaxial-ellipsoidal satellites ($1 > \alpha > \beta$)

$$A_1 = \frac{2\alpha\beta}{(1-\alpha^2)\sqrt{1-\beta^2}}\left(F(r,s) - E(r,s)\right) \tag{15a}$$

$$\text{and} \quad A_3 = \frac{2\alpha\beta}{(\alpha^2-\beta^2)\sqrt{1-\beta^2}}\left(\frac{\alpha}{\beta}\sqrt{1-\beta^2} - E(r,s)\right), \tag{15b}$$

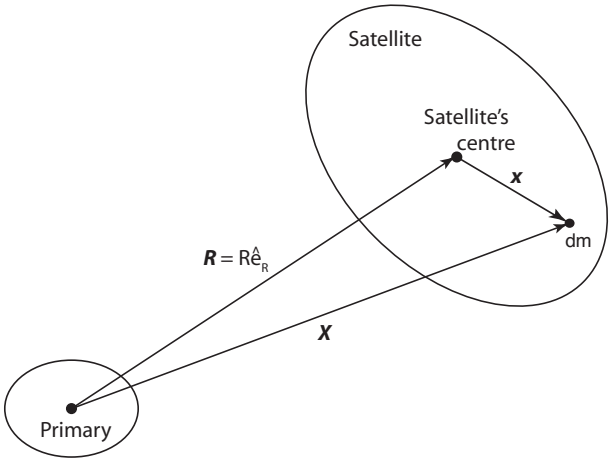


Fig. 2. An ellipsoidal satellite of an ellipsoidal primary. A general configuration showing the quantities involved in the calculation of Sec. 2.3. The figure is *not* to scale.

where $F$ and $E$ are elliptic integrals of the first and second kinds (Abramowitz and Stegun 1965), respectively, with the argument $r = \sqrt{1-\beta^2}$ and parameter $s = \sqrt{(1-\alpha^2)/(1-\beta^2)}$. In each case, we provide only two of the $A_i$, as the third component may be calculated from the relation (Chandrasekhar 1969)

$$A_1 + A_2 + A_3 = 2. \tag{16}$$

### *2.3 Quadrupole moment tensor*

Sharma et al. (2006) calculate $\boldsymbol{M}_Q$ due to a spherical primary. We follow a similar path to develop a formula valid for a triaxial-ellipsoidal primary. The calculation is complicated by the fact that there are many possible relative orientations of the primary and the satellite. Thus, the components of vectors and tensors depend on whether we view them in the primary's ($P$) or the satellite's ($S$) principal-axes coordinate system. In keeping with the notation employed in Appendix A, we will use primes ($'$) to denote vector and tensor components in $P$. Other quantities relevant to the primary, such as the density $\rho'$, will be similarly labeled. We will proceed by outlining a general formulation, though in Secs. 4 and 5 the final formulae will be specialized to configurations of immediate interest.

Consider the geometry shown in Fig. 2. Employing the theorem on the external force field of a triaxial body (Chandrasekhar 1969, p. 48), we obtain the body force for a unit mass (i.e., the acceleration) located at $\mathsf{X}$ ($= R\hat{\mathsf{e}}_R + \mathsf{x}$) to be

$$\mathsf{b}_Q = \frac{d\mathsf{F}}{dm} = -2\pi\rho' G\boldsymbol{B}\cdot\mathsf{X}, \tag{17}$$

where the symmetric *tidal shape tensor* $\boldsymbol{B}$ depends only on $a'_i$ and $\mathsf{X}$, and captures the effect of the primary's triaxiality on its gravitational field. $\boldsymbol{B}$ is diagonalized in $P$, so that from (A.8) we may write, $\boldsymbol{B} = \Sigma_{i=1}^{3} B'_i \hat{\mathsf{e}}'_i \otimes \hat{\mathsf{e}}'_i$ in terms of $\boldsymbol{B}$'s components $B'_i$ in the system $\hat{\mathsf{e}}'_i$. On the other hand, in $S$, the symmetric $\boldsymbol{B}$ in general has its full set of six components $B_{ij}$, i.e., $\boldsymbol{B} = B_{ij}\hat{\mathsf{e}}_i \otimes \hat{\mathsf{e}}_j$. Formulae may be developed for the components $B'_i$ for triaxial ellipsoids by appealing to their integral definitions (Chandrasekhar 1969),

$$B'_i = \int_{\lambda'}^{\infty} \frac{a'_1 a'_2 a'_3 \, du}{\Delta'(a_i'^2 + u)}, \tag{18}$$

where $\Delta' = \sqrt{(a_1'^2 + u)(a_2'^2 + u)(a_3'^2 + u)}$, and the above integral's lower limit $\lambda'$ is the ellipsoidal coordinate of the point $\mathsf{x}'$, i.e., the greatest solution of the equation

$$\frac{X_1'^2}{a_1'^2 + \lambda'} + \frac{X_2'^2}{a_2'^2 + \lambda'} + \frac{X_3'^2}{a_3'^2 + \lambda'} = 1. \tag{19}$$

Thus, because $x_i$ and $X'_i$ are related, $\lambda'$ is a function of $x_i$. Note also that the $B'_i$ depend on $\mathsf{x}$ only through $\lambda'$. Sections 4 reports $B'_i$ for oblate primaries. Knowing the rotation tensor $\boldsymbol{T}$ fixing the satellite's orientation relative to the primary, we can extract $B_{ij}$ from $B'_i$ via the formula (A.11b).

Substituting (17) in (7), we have

$$\boldsymbol{M}_Q = -2\pi\rho' G \left( \int_V \mathsf{x} \otimes \mathsf{x} \cdot \boldsymbol{B} \rho dV + \int_V \mathsf{x} \otimes R\hat{\mathsf{e}}_R \cdot \boldsymbol{B} \rho dV \right), \tag{20}$$

where we have employed the fact that $\mathsf{X} = \mathsf{x} + R\hat{\mathsf{e}}_R$, the formula $\mathsf{a} \otimes (\boldsymbol{C} \cdot \mathsf{b}) = \mathsf{a} \otimes \mathsf{b} \cdot \boldsymbol{C}^T$ for vectors $\mathsf{a}$ and $\mathsf{b}$ and tensor $\boldsymbol{C}$, and the symmetry of $\boldsymbol{B}$.

As for a spherical primary in Sharma et al. (2006), because $\boldsymbol{B}$ depends on $\mathsf{x}$ through $\lambda'$, in order to compute $\boldsymbol{M}_Q$ we will expand $\boldsymbol{B}$ about its value at the satellite's center, i.e., $\mathsf{x} = 0$, retaining terms only up to $O(x_i^2/R^2)$. This seems reasonable, as for most practical problems the satellite is much smaller than its separation from the primary. We therefore approximate the components $B_{ij}$ of $\boldsymbol{B}$ in the satellite's principal axes system $\hat{\mathsf{e}}_i$ as

$$B_{ij} \approx B_{ij}^{(0)} + B_{ijk}^{(1)} \frac{x_k}{R} + B_{ijkl}^{(2)} \frac{x_k x_l}{R^2}, \tag{21}$$

where the coefficients on the right hand side are obtained by appropriately expanding the formulae for $B_{ij}$. Introducing the notation $\boldsymbol{\mathcal{B}}^{(1)}$ and $\mathsf{B}^{(2)}$ for the third and fourth order tensors in the above expansion, respectively, and following Sec. 2.4, we have the coordinate-independent representation

$$\boldsymbol{B} \approx \boldsymbol{B}^{(0)} + \boldsymbol{\mathcal{B}}^{(1)} \cdot \frac{\mathsf{x}}{R} + \mathsf{B}^{(2)} : \frac{\mathsf{x} \otimes \mathsf{x}}{R^2}. \tag{22}$$

Because $\boldsymbol{B}$ is symmetric, so too are the tensors $\boldsymbol{B}^{(0)}$, $\boldsymbol{\mathcal{B}}^{(1)}$ and $\mathsf{B}^{(2)}$ in their first

two arguments, i.e., $B^{(0)}_{ij} = B^{(0)}_{ji}$, $B^{(1)}_{ijk} = B^{(1)}_{jik}$ and $B^{(2)}_{ijkl} = B^{(2)}_{jikl}$. Employing the above expansion in (20) we find that

$$\boldsymbol{M}_Q = -2\pi\rho' G \left[ \int_V \mathsf{x} \otimes \mathsf{x} \cdot \boldsymbol{B}^{(0)} \rho dV + \int_V \mathsf{x} \otimes R\hat{\mathsf{e}}_R \cdot \left( \boldsymbol{\mathcal{B}}^{(1)} \cdot \frac{\mathsf{x}}{R} \right) \rho dV \right],$$

where we have appealed to the definition of the satellite's center of mass, and symmetry arguments to set the integrals with an odd number of $\mathsf{x}$'s to zero. Note that $\mathsf{B}^{(2)}$ does not play a role in the above equation. Following standard tensor manipulation introduced in Appendix A, we simplify the above equation to recover the basis-independent formula

$$\boldsymbol{M}_Q = -2\pi\rho' G \boldsymbol{I} \cdot \left[ \boldsymbol{B}^{(0)} + \left( \hat{\mathsf{e}}_R \cdot \boldsymbol{\mathcal{B}}^{(1)} \right)^T \right]. \tag{23}$$

Recall that $\hat{\mathsf{e}}_R \cdot \boldsymbol{\mathcal{B}}^{(1)}$ is a second-order tensor. We note that while $\boldsymbol{I}$ is diagonalized in the principal axes system of the satellite, $\boldsymbol{B}$, and so consequently, $\boldsymbol{B}^{(0)}$ and $\boldsymbol{\mathcal{B}}^{(1)}$ are diagonal when viewed in $P$. It is helpful to specialize the above expression to the case of a spherical primary of radius $a'$. Then, $\boldsymbol{B}^{(0)}$ and $\boldsymbol{\mathcal{B}}^{(1)}$ are

$$\boldsymbol{B}^{(0)} = \frac{2}{3}\frac{a'^3}{R^3}\boldsymbol{1} \quad \text{and} \quad \boldsymbol{\mathcal{B}}^{(1)} = -2\frac{a'^3}{R^3}\boldsymbol{1} \otimes \hat{\mathsf{e}}_R, \tag{24}$$

and we obtain for $a'_1 = a'_2 = a'_3 = a'$,

$$\boldsymbol{M}_Q^{spherical} = -G\frac{4\pi a'^3}{3R^3}\rho' \boldsymbol{I} \cdot [\boldsymbol{1} - 3\hat{\mathsf{e}}_R \otimes \hat{\mathsf{e}}_R].$$

as obtained earlier by Sharma et al. (2006).

In order to employ the formula (23) profitably, we must develop expressions for $\boldsymbol{B}^{(0)}$ and $\boldsymbol{\mathcal{B}}^{(1)}$. To this end we first calculate the $B'_i$ by integrating (18). From these, $\boldsymbol{B}$'s components in $S$, the $B_{ij}$, are obtained by appealing to the rotation tensor that relates the satellite's and primary's coordinate systems $S$ and $P$, respectively. The $B_{ij}$ are then expanded about the satellite's center $\mathsf{x} = 0$ to yield the tensors $\boldsymbol{B}^{(0)}$ and $\boldsymbol{\mathcal{B}}^{(1)}$. This process will become clear in Sec. 4 when we investigate a particular satellite-primary configuration.

### *2.4 Orbital motion*

The satellite's orbital motion is governed by the primary's gravitational attraction. The total external gravitational force acting on the satellite is obtained by integrating (17),

$$\mathsf{F} = \int_V \frac{d\mathsf{F}}{dm} dm = \int_V \mathsf{b}_Q \rho dV = -2\pi\rho' G \int_V \boldsymbol{B} \cdot \mathsf{X} \rho dV.$$

Setting $\mathsf{X} = R\hat{\mathsf{e}}_R + \mathsf{x}$, expanding $\boldsymbol{B}$ according to (22), substituting into the above and integrating as in the previous section, we arrive at

$$\mathsf{F} = -2\pi\rho' G\left[m\boldsymbol{B}^{(0)}\cdot R\hat{\mathsf{e}}_R + \frac{1}{R}\boldsymbol{\mathcal{B}}^{(1)} : \boldsymbol{I} + \frac{1}{R}\left(\mathsf{B}^{(2)} : \boldsymbol{I}\right)\cdot\hat{\mathsf{e}}_R\right],$$

with $m$ being the satellite's mass. As it follows its circular orbit around the massive primary, the satellite's centripetal acceleration must be sustained by $\hat{\mathsf{e}}_R\cdot\mathsf{F}$, so that we obtain the orbital angular velocity as

$$\omega^2 = 2\pi\rho' G\hat{\mathsf{e}}_R\cdot\left[\boldsymbol{B}^{(0)}\cdot\hat{\mathsf{e}}_R + \frac{1}{mR^2}\left(\boldsymbol{\mathcal{B}}^{(1)} + \hat{\mathsf{e}}_R\cdot\mathsf{B}^{(2)}\right) : \boldsymbol{I}\right], \tag{25}$$

where we have employed the symmetry of $\mathsf{B}^{(2)}$ in its first two indices to simplify the above expression. In the above, we have again neglected the satellite's effect on the primary, taking the latter to be essentially fixed. In future applications to binary systems, where the components are often of comparable masses, it will be necessary to include also the primary's motion. We note that, this time, the tensors $\boldsymbol{B}^{(0)}$, $\boldsymbol{\mathcal{B}}^{(1)}$ and $\mathsf{B}^{(2)}$ are required. For a tidally-locked satellite, the orbital angular velocity equals its rotation rate, so that once $\omega$ is known from the above, the spin tensor $\boldsymbol{W}$ associated with the rotation rate may be constructed.

In the above formula, the first term is what would result if we assumed that all the satellite's mass were located at its center. The next two terms bring in the effect of the satellite's distributed mass on its orbital motion. Typically, this is a weak perturbation, as evinced by the presence of $R^2$ in the denominator, and we comment on its magnitude in the next subsection.

### *2.5 Non-dimensionalization*

Collecting together (10), (12) and (23) we arrive at

$$\boldsymbol{\sigma} = \frac{1}{V}\left[-2\pi\rho G\boldsymbol{A}\cdot\boldsymbol{I} - 2\pi\rho' G\left(\boldsymbol{B}^{(0)} + \hat{\mathsf{e}}_R\cdot\boldsymbol{\mathcal{B}}^{(1)}\right)\cdot\boldsymbol{I} - \boldsymbol{W}^2\cdot\boldsymbol{I}\right],$$

which provides the average stress in a tidally-locked *triaxial* satellite located on a *circular* orbit by $\hat{\mathsf{e}}_R$ with respect to a *triaxial* primary. The first term on the right is the average stress due to the satellite's internal gravity, the second is the average tidal stress introduced by the primary, while the last is the average "centrifugal" stress. We non-dimensionalize the above equation by rescaling time by $1/\sqrt{2\pi\rho G}$, and the stress by $(3/20\pi)(2\pi\rho G m)(4\pi/3V)^{1/3}$, where $\rho, V$ and $m$ are the satellite's density, volume and mass, respectively.

We obtain

$$\boldsymbol{\sigma} = -(\alpha\beta)^{-2/3}\left[\boldsymbol{W}^2 + \boldsymbol{A} + \frac{1}{\eta}\left(\boldsymbol{B}^{(0)} + \hat{\mathsf{e}}_R \cdot \boldsymbol{\mathcal{B}}^{(1)}\right)\right] \cdot \boldsymbol{Q}, \tag{26}$$

where $\alpha$ and $\beta$ are the satellite's axes ratios, $\eta = \rho/\rho'$ is the ratio of the satellite's to the primary's density, $\boldsymbol{W}$ and $\boldsymbol{\sigma}$ now represent the non-dimensional spin and average stress tensors, respectively, and $\boldsymbol{Q}$ is a non-dimensional tensor derived from the inertia tensor. In $S$, $\boldsymbol{Q}$ takes the form

$$[\boldsymbol{Q}] = \begin{pmatrix} 1 & 0 & 0 \\ 0 & \alpha^2 & 0 \\ 0 & 0 & \beta^2 \end{pmatrix}, \tag{27}$$

where, recall from Appendix A that square brackets denote evaluation of a tensor in a coordinate system, in this case the satellite's.

Similarly, we non-dimensionalize (25) to obtain

$$\omega^2 = \frac{1}{\eta}\,\hat{\mathsf{e}}_R \cdot \left[\boldsymbol{B}^{(0)} \cdot \hat{\mathsf{e}}_R + \frac{1}{5q'^2}\left(\frac{\kappa\alpha'\beta'}{\eta\alpha\beta}\right)^{2/3}\left(\boldsymbol{\mathcal{B}}^{(1)} + \hat{\mathsf{e}}_R \cdot \mathsf{B}^{(2)}\right) : \boldsymbol{Q}\right], \tag{28}$$

where now $\omega$ is the scaled orbital angular velocity that equals a tidally-locked satellite's spin, $\kappa = m/m'$ is the ratio of the satellite's to the primary's mass, and $q' = R/a'_1$ is the scaled orbital radius. In the present application we have assumed that the primary is much more massive than the satellite, i.e., $\kappa \ll 1$, and consequently we drop the corrective second-order terms, to obtain

$$\omega^2 \approx \frac{1}{\eta}\,\hat{\mathsf{e}}_R \cdot \boldsymbol{B}^{(0)} \cdot \hat{\mathsf{e}}_R. \tag{29}$$

Note that the scaled orbit size $q'$ may yet be an $O(1)$ quantity. We emphasize that the above formula, through $\boldsymbol{B}^{(0)}$, retains the effect of the primary's ellipsoidal nature on the satellite's orbital motion; dropping the second-order terms in (28) is equivalent to neglecting the effect of the secondary's distributed mass.

Finally, we again make contact to the case of a spherical primary by setting $a'_1 = a'_2 = a'_3 = a'$. Using (24) in the above equation to find

$$\omega^2 \approx \frac{1}{\eta}\,\hat{\mathsf{e}}_R \cdot \frac{2}{3}\frac{a'^3}{R^3}\boldsymbol{1} \cdot \hat{\mathsf{e}}_R = \frac{2}{3}\frac{\rho'}{\rho}\frac{a'^3}{R^3},$$

the expected (approximate) formula for the non-dimensional orbital angular velocity of a satellite on a circular orbit about a massive spherical primary.

In a tidally-locked configuration, we orient the satellite's longest principal axis $\hat{\mathsf{e}}_1$ to point away from the primary (see, e.g., Fig. 3). The principal axis $\hat{\mathsf{e}}_3$ is taken to be normal to the orbital plane. This fixes the satellite's principal axes system $S$. We will evaluate both (26) and (29) in $S$. The form of the tensor $\boldsymbol{Q}$ in $S$ is given above in (27). The gravitational shape tensor $\boldsymbol{A}$ is diagonal in $S$, i.e.,

$$[\boldsymbol{A}] = \begin{pmatrix} A_1 & 0 & 0 \\ 0 & A_2 & 0 \\ 0 & 0 & A_3 \end{pmatrix}, \tag{30}$$

where, depending on the satellite's shape, $A_1, A_2$ and $A_3$ are given by either of (13), (14), or (15), along with (16). The non-dimensional spin tensor becomes

$$[\boldsymbol{W}] = \begin{pmatrix} 0 & -W_3 & 0 \\ W_3 & 0 & 0 \\ 0 & 0 & 0 \end{pmatrix}, \tag{31}$$

where, because the satellite is tidally locked,

$$W_3^2 = \omega^2 \approx \frac{1}{\eta}\, \hat{\mathsf{e}}_R \cdot \boldsymbol{B}^{(0)} \cdot \hat{\mathsf{e}}_R \tag{32}$$

after substituting for $\omega$ from (29). We have neglected any "roll" about the axis that points towards the primary. Note that $W_3$ depends on the primary's orientation with respect to the satellite and simplified expressions for it will be obtained separately for the two cases considered later. The tidal shape tensor $\boldsymbol{B}$'s matrix and so also those of $\boldsymbol{B}^{(0)}$, $\boldsymbol{\mathcal{B}}^{(1)}$ and $\mathsf{B}^{(2)}$, similarly depend on the orientation of the primary's principal axes system $P$, and will be derived for the example configuration in Sec. 4. Finally, the stress tensor's components in $S$ will be taken to be $\sigma_{ij}$.

The *exact* volume-averaged stresses in a *tidally-locked*, *triaxial*-ellipsoidal satellite as it moves in a *circular* orbit about a *triaxial* ellipsoidal primary are given by (26). However, these stresses cannot take arbitrary values for rubble piles that yield under high-enough shear stresses. The next section introduces a yield criterion for such granular aggregates that will help put bounds on the possible shape and density that a rubble-pile satellite at a distance $q'$ from a primary may achieve before it disrupts.

## 3 Rheology

Cohesionless rubble piles/granular aggregates (think of a gravel pile) are primarily characterized by their inability to withstand tensile stress and also their non-zero, but finite, resistance to shear stresses. This ability to support shear stresses is traced to both the usual interfacial friction due to particle interaction, as well as a geometric friction due to interlocking of finite-sized constituents. Because of its frictional roots, the shear resistance of rubble piles depends on internal pressure. It is further noticed that granular materials when compressively loaded, suffer minimal deformation until a critical load is reached, beyond which they deform rapidly. Keeping these features in mind, it is quite common to model granular aggregates, in the first instance, as rigid perfectly-plastic materials with an appropriate pressure-dependent yield criterion; see, e.g., Schaeffer (1987). Because here we are concerned with only equilibrium shapes, and not dynamical behavior post-yield, we will only introduce yield criteria relevant for a granular aggregate and not model the aggregate's behavior after it yields. More complete discussions of modeling granular materials as rigid perfectly-plastic materials, addressing also their post-yield flow, are provided in Sharma (2004) and Sharma et al. (2008).

Pressure-dependent yield criteria appropriate for granular materials are provided by both the Mohr-Coulomb and the Drucker-Prager failure laws (Chen and Han 1988). The Mohr-Coulomb yield criterion is stated in terms of the extreme principal stresses

$$\sigma_{max} - k_{MC}\sigma_{min} \leq 0, \tag{33}$$

where $k_{MC}$ is related to the internal friction angle $\phi_F$ by

$$k_{MC} = \frac{1 + \sin\phi_F}{1 - \sin\phi_F}. \tag{34}$$

Here, we prefer to employ the Drucker-Prager yield criterion as its smoothness facilitates numerical calculations, though a brief comparison with the results of a Mohr-Coulomb material is provided in Sec. 6.2. To formulate the Drucker-Prager failure rule we define the pressure $p$

$$p = -\frac{1}{3}\text{tr}\,\boldsymbol{\sigma}, \tag{35}$$

where 'tr' denotes the trace of the tensor, and the deviatoric stress $\boldsymbol{s}$

$$\boldsymbol{s} = \boldsymbol{\sigma} + p\mathbf{1}. \tag{36}$$

The Drucker-Prager yield condition can then be written as

$$|\boldsymbol{s}|^2 \leq k^2 p^2, \tag{37}$$

where $|\boldsymbol{s}|$ indicates the magnitude of the deviatoric stress as given by

$$|\boldsymbol{s}|^2 = s_{ij}s_{ij},$$

applying the summation convention, and

$$k = \frac{2\sqrt{6}\sin\phi_F}{3-\sin\phi_F}, \tag{38}$$

defined so that the Drucker-Prager yield surface is the outer envelope of the Mohr-Coulomb yield surface corresponding to the same friction angle $\phi_F$. As the friction angle lies between $0^o$ and $90^o$, $0 \geqslant k \geqslant \sqrt{6}$. Finally, in terms of the three principal stresses $\sigma_i$, the definition above for $|\boldsymbol{s}|$ may be put into the illuminating form

$$|\boldsymbol{s}|^2 = \frac{1}{3}\left[(\sigma_2-\sigma_3)^2+(\sigma_3-\sigma_1)^2+(\sigma_1-\sigma_2)^2\right] = \frac{2}{3}\left(\tau_1^2+\tau_2^2+\tau_3^2\right), \tag{39}$$

where $\tau_i = (\sigma_j - \sigma_k)/2,\ (i \neq j \neq k)$ are the principal *shear* stresses at a point. Thus, $|\boldsymbol{s}|$ may be thought of as a measure of the "total" local shear stress. Thus, the Drucker-Prager yield criterion (37), along with (38), puts a limit on the allowable local shear stresses in terms of the local pressure and the internal friction angle. This interpretation will be found useful when we explore the yielding modes of tidally-locked satellites later.

## 4 Example: Satellites of oblate primaries

We now commence to explore the equilibrium landscape of rubble-pile satellites. So far we have at most assumed that the tidally-locked satellite follows a circular path around an ellipsoidal primary. For clarity, we will now restrict ourselves to the geometry shown in Fig. 3, viz., an oblate primary with the triaxial-ellipsoidal satellite's orbit lying in the primary's equatorial plane. Recall that for a tidally-locked configuration to be stable, the satellite's long-axis $a_1$ must point towards the primary. This configuration is of immediate importance for planetary satellites.

The average value of the stresses evaluated in $S$ within a tidally-locked ellipsoidal satellite on a circular orbit is obtained from (26) along with (27), (30), (15) (or (13), or (14)), (31) and (32). In addition, we require expressions for the tensors $\boldsymbol{B}^{(0)}$ and $\boldsymbol{\mathcal{B}}^{(1)}$ in the satellite's principal coordinate system. These two tensors are obtained according to the prescription outlined in the last paragraph of Sec. 2.3, and will be apparent in the following section. Note that because we have used the approximate expression (32) for $W_3$ rather than (28), we will not require $\mathsf{B}^{(2)}$. The stresses finally obtained, along with the yield

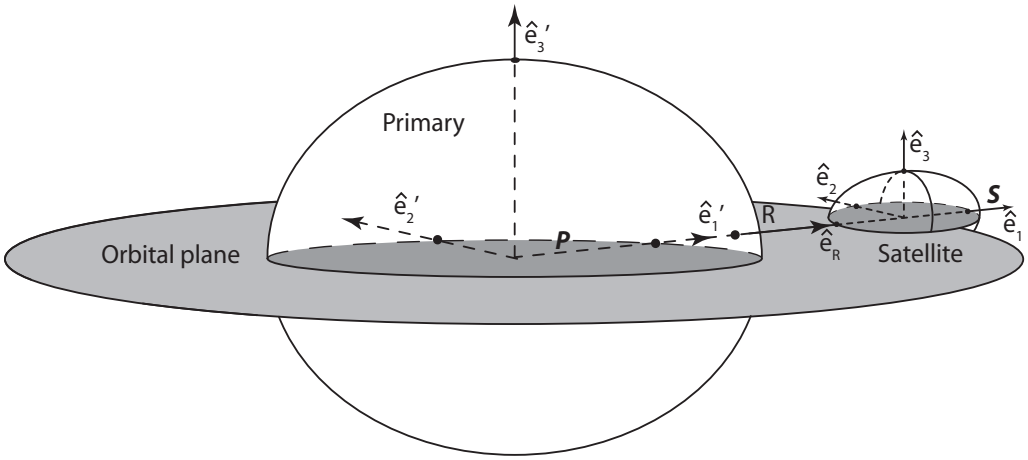


Fig. 3. An ellipsoidal satellite of an oblate primary. The axes $\hat{\mathsf{e}}'_i$ of $P$ and $\hat{\mathsf{e}}_i$ of $S$ coincide. The orbital plane is normal to $\hat{\mathsf{e}}_3$. The unit vector $\hat{\mathsf{e}}_R$, parallel to $\hat{\mathsf{e}}_1$, locates the satellite with respect to the primary's center.

criterion (37), will help generate bounds that delineate a rubble-pile satellite's equilibrium landscape as a function of its shape, the primary's shape, their relative density, and the orbit's size. Recall that in a tidally-locked scenario, the latter is linked to the satellite's spin via (32).

In Fig. 3, the primary is an oblate ellipsoid, possibly a planet, with $a'_1 = a'_2 \geqslant a'_3$, and the ellipsoidal satellite ($a_1 \geqslant a_2 \geqslant a_3$) is located a distance $R$ along the primary's $\hat{\mathsf{e}}'_1$ axis, with its long-axis $a_1$ pointing towards the primary. Both the primary's and the satellite's third axes are taken to be normal to the orbital plane. With these choices, Fig. 3 shows that $\hat{\mathsf{e}}'_i$ and $\hat{\mathsf{e}}_i$ are the same, and the rotation tensor $\boldsymbol{T}$ relating $P$ and $S$ is simply an identity tensor, i.e.,

$$\boldsymbol{T} = \boldsymbol{1}. \tag{40}$$

We also see that $\hat{\mathsf{e}}_R = \hat{\mathsf{e}}_1$. We are now in a position to obtain $\boldsymbol{B}^{(0)}$ and $\boldsymbol{\mathcal{B}}^{(1)}$.

### *4.1* $\boldsymbol{B}^{(0)}$ *and* $\boldsymbol{\mathcal{B}}^{(1)}$

The components $B'_i$ for an oblate primary, i.e., $a'_1 = a'_2 \geqslant a'_3$, are found after integrating (18) to be

$$B'_1 = B'_2 = \frac{a_1'^2 a'_3}{p_2'^3}\left(\frac{\pi}{2} - p'_2\frac{\sqrt{a_3'^2+\lambda'}}{a_1'^2+\lambda'} - \tan^{-1}\frac{\sqrt{a_3'^2+\lambda'}}{p'_2}\right) \tag{41a}$$

$$\text{and} \quad B'_3 = -\frac{2a_1'^2 a'_3}{p_2'^3}\left(\frac{\pi}{2} - p'_2\frac{1}{\sqrt{a_3'^2+\lambda'}} - \tan^{-1}\frac{\sqrt{a_3'^2+\lambda'}}{p'_2}\right), \tag{41b}$$

where $p_2' = \sqrt{a_1'^2 - a_3'^2}$, and the ellipsoidal coordinate $\lambda'$ is given by (19). Note that upon dividing by $a_1'^3$ we can express (41) in terms of the scaled orbital radius $q\,(= R/a_1')$ and the primary's axes ratio $\beta'$ $(= a_3'/a_1')$. Employing (40) with the tensor coordinate transformation formulae (A.11b), we obtain

$$B_{ij} = B_i'\delta_{ij} \quad \text{(no sum)}, \tag{42}$$

i.e., because $P$ and $S$ are identical, so too are $\boldsymbol{B}$'s components in them.

We next solve (19) approximately to find $\lambda'$ at a point $\mathsf{X} = \mathsf{x} + R\hat{\mathsf{e}}_1$ within the satellite. To this end we note from Fig. 3 (or, equivalently (40) and (A.11a)) that $x_i = x_i'$. To order $x_i^2/R^2$, we obtain

$$\lambda' = \lambda'(\mathsf{x}) \approx \lambda_0' + R^2\left\{2\frac{x_1}{R} + \frac{1}{R^2}\left(x_1^2 + x_2^2 + \frac{R^2}{R^2 - p_2'^2}\,x_3^2\right)\right\}, \tag{43}$$

where

$$\lambda_0' = R^2 - a_1'^2 \tag{44}$$

is the value of $\lambda'$ at the satellite's center, i.e., at $\mathsf{x} = 0$. We substitute the above approximation into the formulae for $B_{ij}$ obtained from (42) and (41), and expand up to $O(x_i^2/R^2)$ to find an expression similar to (21). This yields the components of the tensors $\boldsymbol{B}^{(0)}$, $\boldsymbol{\mathcal{B}}^{(1)}$ and $\mathsf{B}^{(2)}$ in $S$, the satellite's coordinate system. In particular, $\boldsymbol{B}^{(0)}$ is diagonal with $B_{ii}^{(0)} = B_i'|_{\lambda'=\lambda_0'}$, so that (41) yields

$$\begin{aligned} B_{11}^{(0)} = B_{22}^{(0)} &= \frac{\beta'}{(1-\beta'^2)^{3/2}}\left(\frac{\pi}{2} - \frac{q_o'\sqrt{(1-\beta'^2)}}{q'^2} - \tan^{-1}\frac{q_o'}{\sqrt{1-\beta'^2}}\right) \qquad (45a)\\ &\approx \frac{2}{3}\frac{\beta'}{q'^3} + \frac{1}{5}\frac{\beta'(1-\beta'^2)}{q'^5} + \frac{3}{28}\frac{\beta'(1-\beta'^2)^2}{q'^7}... \\ \text{and}\quad B_{33}^{(0)} &= -\frac{2\beta'}{(1-\beta'^2)^{3/2}}\left(\frac{\pi}{2} - \frac{\sqrt{1-\beta'^2}}{q_o'} - \tan^{-1}\frac{q_o'}{\sqrt{1-\beta'^2}}\right), \qquad (45b)\\ &\approx \frac{2}{3}\frac{\beta'}{q'^3} + \frac{3}{5}\frac{\beta'(1-\beta'^2)}{q'^5} + \frac{15}{28}\frac{\beta'(1-\beta'^2)^2}{q'^7}... \end{aligned}$$

where we have chosen to express quantities in terms of the primary's axes ratio $\beta'$, the satellite's scaled orbital radius $q'$, and $q_o'^2 = q'^2 + \beta'^2 - 1$. Similarly, the only non-zero components of $\boldsymbol{\mathcal{B}}^{(1)}$ are

$$\begin{aligned} B_{111}^{(1)} = B_{221}^{(1)} &= -\frac{2\beta'}{q'^2 q_o'} \approx -2\frac{\beta'}{q'^3} - \frac{\beta'(1-\beta'^2)}{q'^5} - \frac{3}{4}\frac{\beta'(1-\beta')^2}{q'^7} + ... \qquad (46a)\\ \text{and}\quad B_{331}^{(1)} &= -\frac{2\beta'}{q_o'^3} \approx -2\frac{\beta'}{q'^3} - 3\frac{\beta'(1-\beta'^2)}{q'^5} - \frac{15}{4}\frac{\beta'(1-\beta')^2}{q'^7} + ....\qquad (46b) \end{aligned}$$

In the above, we have provided expansions in orders of $1/q'$ to illustrate that the oblateness $\beta'$ enters linearly at the first order. For $\beta' \approx 1$ and/or large

enough $q'$'s, as is the case with most known planetary satellite systems, retaining only the first terms is found sufficient (see Sec. 5). This simplification prompts the introduction of an *equivalent distance* $\overline{q}' = q' \left(\eta/\beta'\right)^{1/3}$ that, in the leading-order approximation, absorbs the effect of the density ratio $\eta$ and the primary's axes ratio $\beta'$. However, in Sec. 4.3, we will investigate the equilibrium landscape while employing the exact expressions for $B_{ij}^{(0)}$ and $B_{ijk}^{(1)}$ provided above. In this case, $\overline{q}'$ does not capture the effects of $\eta$ and $\beta'$ in their entirety, but because it does do so to first order, we will express results in terms of $\overline{q}'$ rather than $q'$.

### *4.2 The spin $W_3$*

With $\hat{\mathsf{e}}_R = \hat{\mathsf{e}}_1$, from (32), we obtain

$$W_3^2 = \frac{1}{\eta} B_{11}^{(0)}, \tag{47}$$

with $B_{11}^{(0)}$, given by (45a), capturing the effect of the primary's asphericity.

### *4.3 Equilibrium landscape*

We proceed to explore the equilibrium of an *oblate* primary's rubble-pile satellite, as shown in Fig. 3. To this end, we utilize (26) to express the average stresses within the satellite in its principal axes system $\hat{\mathsf{e}}_i$. We find

$$\begin{aligned}
\sigma_1 &= -\left\{-W_3^2 + A_1 + \frac{1}{\eta}\left(B_{11}^{(0)} + B_{111}^{(1)}\right)\right\}(\alpha\beta)^{-2/3}, \\
\sigma_2 &= -\alpha^2\left(-W_3^2 + A_2 + \frac{1}{\eta}B_{11}^{(0)}\right)(\alpha\beta)^{-2/3} \\
\text{and} \quad \sigma_3 &= -\beta^2\left(A_3 + \frac{1}{\eta}B_{33}^{(0)}\right)(\alpha\beta)^{-2/3},
\end{aligned}$$

where $\eta = \rho/\rho'$ is the density ratio, $\alpha$ and $\beta$ the satellite's axes ratios, and the expressions for $A_i$ are given by appropriate formulae in Sec. 2.2, while those of $B_{ij}^{(0)}$ and $B_{ijk}^{(1)}$ by (45) and (46), respectively. The primary's oblateness $\beta'$ and the size of the satellite's orbit $q'$ (or, equivalently, $\overline{q}'$) affect the stresses through the terms $B_{11}^{(0)}$, $B_{33}^{(0)}$ and $B_{111}^{(1)}$. On substituting for $W_3$ from (47), the

above expressions simplify further to become

$$\sigma_1 = -\left(A_1 + \frac{1}{\eta} B_{111}^{(1)}\right)(\alpha\beta)^{-2/3}, \tag{49a}$$

$$\sigma_2 = -\alpha^2 A_2 (\alpha\beta)^{-2/3} \tag{49b}$$

$$\text{and} \quad \sigma_3 = -\beta^2 \left(A_3 + \frac{1}{\eta} B_{33}^{(0)}\right)(\alpha\beta)^{-2/3}. \tag{49c}$$

The stresses above must satisfy the Drucker-Prager yield criterion (37) in order for the satellite to exist in equilibrium. At equilibrium, equality holds in (37), thereby providing a relationship between the satellite's axes ratios $\alpha$ and $\beta$, its internal friction angle $\phi_F$, the equivalent orbit size $\overline{q}'$, the primary's oblateness $\beta'$, and the density ratio $\eta$. The satellite's equilibrium is thus governed by several variables. The aim is to identify the limits placed on the satellite's orbital radius $q'$ by the remaining five parameters $\phi_F, \alpha, \beta, \beta'$ and $\eta$. This is a high-dimensional and complicated relationship, and we will explore it graphically by taking appropriate two-dimensional sections.

We first fix the primary's oblateness $\beta'$ at 0.8 and the density ratio $\eta$ to 0.5. The satellite is thus half as dense as the primary. With these choices, $q' \approx 1.17\,\overline{q}'$. The critical equivalent orbital radius $\overline{q}'$ is now regulated only by the satellite's shape in terms of its axes ratios $\alpha$ and $\beta$, and the internal friction angle $\phi_F$. At any given $\phi_F$, the set of $\overline{q}'$, $\alpha$ and $\beta$ that ensure the satellite's equilibrium, i.e., produce (average) stresses that do not violate the yield criterion, define a three-dimensional region in $\alpha - \beta - \overline{q}'$ space. Different $\phi_F$ yield different regions. For each friction angle, the *critical* surfaces delineating the associated region, provide us with limits on $\overline{q}'$ given the satellites $\alpha$ and $\beta$. Conversely, knowing the orbit's size $\overline{q}'$ constrains the satellite's $\alpha$ and $\beta$. The critical surfaces themselves are obtained by assuming equality in the yield criterion (37). We probe this three-dimensional region via planes obtained by either fixing $\alpha$, or relating $\alpha$ to $\beta$. Thus, each such two-dimensional section, henceforth called an $\alpha$-section, corresponds to a class of self-similar ellipsoidal satellites. Five such planar sections corresponding to $\alpha = 0.5$ and 0.75, and to oblate ($\alpha = 1$), prolate ($\alpha = \beta$) and average-triaxial ($\alpha = (1+\beta)/2$) ellipsoids are shown in Figs. 4 and 5. We discuss them next. We reiterate that while exploring the $\alpha - \beta - \overline{q}'$ space, $\beta' = 0.8$ and $\eta = 0.5$.

In the $\alpha$-sections of Figs. 4 and 5, the critical surfaces corresponding to a friction angle $\phi_F$ now appear as curves. On these curves, $\overline{q}'$ is related only to $\beta$, and this relationship may be obtained from the yield criterion (37) at equality. These curves help define regions in $\beta - \overline{q}'$ space within which a satellite can survive as a rubble pile, provided its internal friction is at least as great as that due to the defining curve's associated $\phi_F$. Thus, for example, a satellite with $\alpha = 0.5$ and a friction value of $\phi_F = 20^o$ may only exist in equilibrium within the shaded region of Fig. 4(a). We also see that the

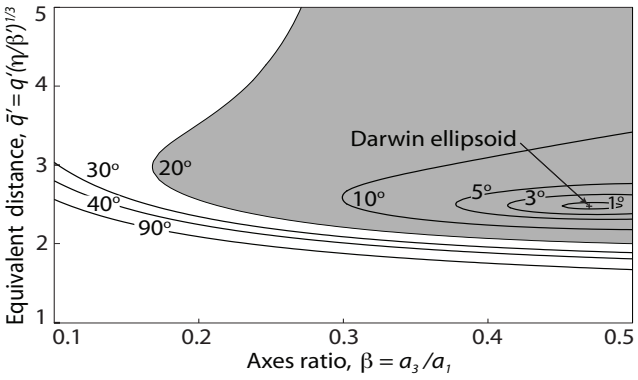


(a) $\alpha = 0.5$

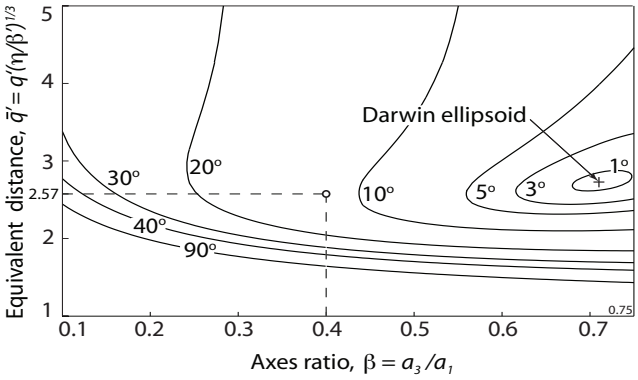


(b) $\alpha = 0.75$

Fig. 4. The equilibrium landscape in $\beta - \overline{q}'$ space as viewed on the sections $\alpha = 0.5$ and 0.75. The number next to a critical curve is the associated friction angle $\phi_F$. The primary's oblateness $\beta' = 0.8$ and the density ratio $\eta = 2$. The axis ratio $\beta$'s upper limit is set by the inequality $\beta \leqslant \alpha$. The Darwin ellipsoid at $\phi_F = 0^o$ is indicated by a '+' symbol.

equilibrium region for any $\phi_F$ encloses those of all smaller friction angles. This simply reflects that increasing internal friction allows the body to withstand greater shear stresses. An important consequence of this is that constraints reflected by equilibrium landscapes such as Figs. 4 and 5 impose *necessary*, but *not sufficient*, requirements on the satellite to persist in equilibrium. This, for example, means that any satellite with given physical and orbital data will require an internal friction at least as great as the $\phi_F$ corresponding to the critical curve that passes through its location in $\beta - \overline{q}'$ space.

In both the $\alpha$-sections shown in Fig. 4, we see that the allowed regions become increasingly smaller as the friction angle decreases, reducing ultimately to a point when $\phi_F$ becomes zero. This is indicated by a '+' symbol. Recall that $\phi_F = 0^o$ corresponds to inviscid fluids, so that this point is, in fact, the

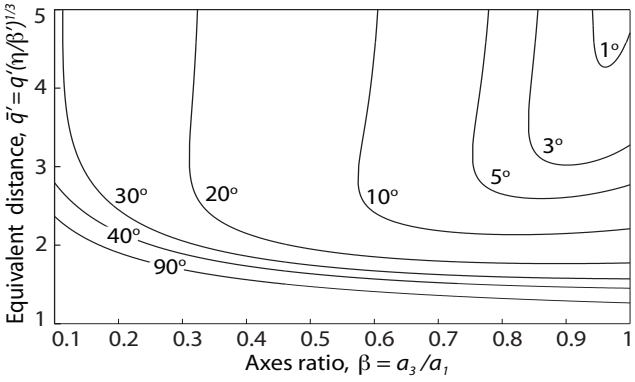


(a) Oblate satellite with $\alpha = 1$

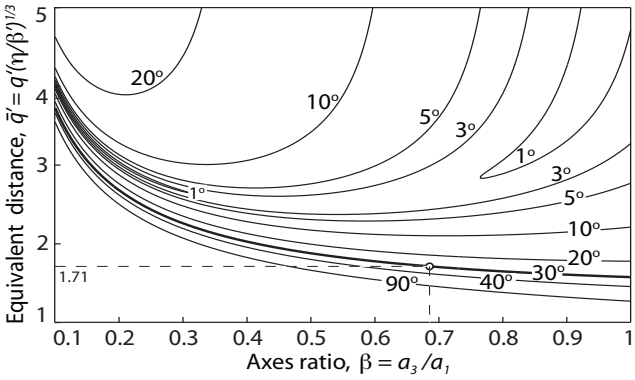


(b) Prolate satellite with $\alpha = \beta$

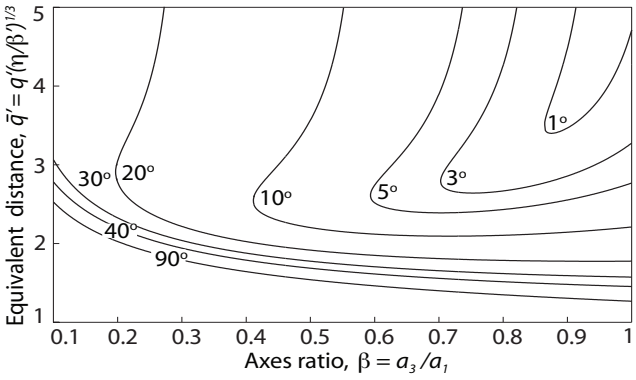


(c) Triaxial satellites with $\alpha = (1 + \beta)/2$

Fig. 5. Continued from Fig. 4. The equilibrium landscape in $\beta - \overline{q}'$ space as viewed on sections corresponding to oblate, prolate and average-triaxial-ellipsoidal satellites. For these shapes, there is no solution at $\phi_F = 0^o$. See also Fig. 4's caption.

intersection of the first Darwin sequence of ellipsoids (Chandraskhar 1969) with the planes $\alpha = 0.5$ or $\alpha = 0.75$. In contrast, note from Fig. 5 that oblate, prolate, or average-triaxial ($\alpha = (1+\beta)/2$), inviscid tidally-locked, fluid ellipsoids do not exist. To be completely precise, the Darwin sequence obtained here is for a primary whose oblateness $\beta'$ is taken fixed and not necessarily related to any spin that the primary may itself have. In the Darwin problem, as considered by Chandrasekhar (1969), the primary was a fluid Maclaurin spheroid. But, because the focus here is on the satellite's equilibrium, we will not belabor this distinction, and instead label the solution obtained for $\phi_F = 0^o$, when it exists, as a Darwin ellipsoid.

For the $\alpha$-sections displayed in Fig. 4, the equilibrium regions are closed at low friction angles. This is not the case at higher $\phi_F$'s, or for any friction value for the oblate/prolate/average-triaxial shapes considered in Fig. 5. Typically, for any $\phi_F$, at a fixed axes ratio $\beta$, there is both a lower and an upper limit to the size of a rubble-pile satellite's orbit. Comparing Figs. 4(a) - 5(c), we also see that for any $\phi_F$, the $\beta$-range over which the upper limit exists, reduces with increasing $\alpha$; the equilibrium regions for the oblate case in Fig. 5(a) have almost no upper bounds. Physically, the lower bound corresponds to failure driven by increased tidal and centrifugal stresses. Closer to the primary, both these forces increase due to stronger tidal interaction with the primary and a higher rotation rate. Thus, we identify this failure mode as *tidal disruption*. This mode has close analogy with the upper rotational disruption curve that occurs in the equilibrium landscape of rubble piles in pure spin (Sharma et al. 2008). The upper bound, on the other hand, is associated with the body's inability to withstand its own gravity. We term this as *gravitational collapse*. At distances far away from the primary, tidal and centrifugal forces reduce. The latter, because the satellite is assumed to be spin-locked. In such conditions, internal gravity comes to dominate, and may cause yielding. This upper bound should be compared with the lower critical curve for spinning rubble piles (Sharma et al. 2008).

Equilibrium regions such as shown in Figs. 4 and 5 are useful to put bounds on the satellite's physical parameters such as shape or internal structure. As a first illustration, consider a satellite with $\alpha = 0.75$ and $\beta = 0.4$ moving on an orbit with $\overline{q}' = 2.57$ about an oblate primary with $\beta' = 0.8$ and $\eta = 0.5$. Such an object may be located on the section of Fig. 4(b), as shown by the filled circle. We see that this body lies outside the $\phi_F = 10^o$ curve but within the region where rubble piles with an internal friction of $\phi_F = 20^o$ may survive. This allows us to conclude that the satellite in question must be composed of a material with a friction angle greater than $10^o$. This could be a rubble pile, as such aggregates typically have $\phi_F \approx 30^o$ (Nedderman 1992, p. 25, Table 3.1). Conversely, if a body's orbit were known, and we were confident about the object being a rubble pile, we could employ sections such as those in Figs. 4 and 5 to constrain its shape. For example, assuming that $\phi_F = 30^o$

is appropriate for granular aggregates, we may conclude from Fig. 5(b) that a tidally-locked rubble pile at a distance $\overline{q}' = 1.71$ from an oblate primary with $\beta' = 0.8$ and $\eta = 0.5$, can be a prolate ellipsoid with $\alpha = \beta \geqslant 0.69$. This is indicated by an open circle in Fig. 5(b). Any smaller $\beta$ would place the satellite outside the $\phi_F = 30^o$ curve, contradicting our assumption about the maximum shear strength of granular aggregates. Finally, if one of the axes ratios were known, a similar analysis may be carried out to constrain the other ratio.

Next, we explore how the satellite's equilibrium landscape is affected by the primary's oblateness $\beta'$. To this end, we restrict the satellite to be either a prolate ($\alpha = \beta$) or an average-triaxial ($\alpha = (1+\beta)/2$) ellipsoid, and also fix the density ratio $\eta$ at 0.5. Figure 6 plots the critical curves corresponding to several friction angles for $\beta'$ equalling 1, 0.8, 0.6 and 0.4. The value $\beta' = 1$ corresponds to a spherical primary, in which case the first Darwin problem reduces to the Roche problem (see Sec. 5). The arrows in Fig. 6 indicate directions of increasing $\beta'$. It is seen that the equilibrium region in $\beta - \overline{q}'$ space remains essentially unchanged, especially at low friction angles. This is due to our employing the equivalent distance $\overline{q}' = q' \left(\eta/\beta'\right)^{1/3}$, which to first order absorbs the effects of both density ratio $\eta$ and the primary's oblateness $\beta'$. That the critical curves do not coincide, but in fact move downwards as the primary becomes "flatter", i.e., $\beta'$ lessens, is due to our employing exact formulae for $B_{ij}^{(0)}$ and $B_{ijk}^{(1)}$; see (45) and (46). Because $\overline{q}' \propto R/a_1'\beta'^{1/3} \propto R\left(\rho'/m'\right)^{1/3}$, we conclude that, in physical space, the critical distance beyond which a satellite with fixed axes ratio $\beta$ may exist increases as the primary flattens, as long as $m'$ and $\rho'$ remain fixed. This may be traced directly to the fact that, for the same mass and density, a flatter primary's in-plane tidal influence persists for greater distances.

The effect of $\beta'$ will have important consequences for satellite systems with significant ring mass, or satellites of flattened asteroids/planets. Typically, though, asteroids tend to be prolate or triaxial rather than oblate, in which case the calculations above need to reworked for prolate/triaxial primaries, in a manner similar to that of an oblate central body.

Finally, we investigate the impact of changing the density ratio $\eta = \rho/\rho'$. This time, we consider only a prolate satellite. The results are shown in Fig. 7(a). The density ratio varies as 0.5, 1, 1.5 and 2, i.e., from a situation where the satellite is half as dense as the primary, to one where it is twice as dense. Both ends of this spectrum are of physical interest. The primary's oblateness $\beta'$ was fixed at 0.8, and four friction angles for each $\eta$ were considered. The arrows in Fig. 7(a) indicate directions of increasing $\eta$. We have truncated critical curves that fell below $q' = 1.1$. We again observe that in $\beta - \overline{q}'$ space, the allowed equilibrium region remains almost unaltered. This, as mentioned earlier, is a reflection of the fact that $\overline{q}'$ absorbs the leading order effect of $\eta$

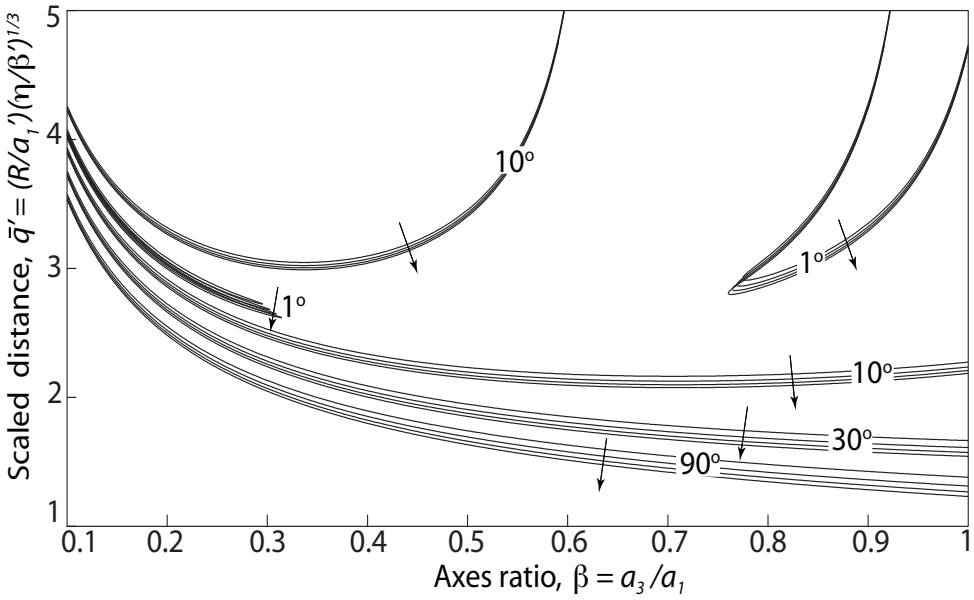


(a) Prolate satellites with $\alpha = \beta$

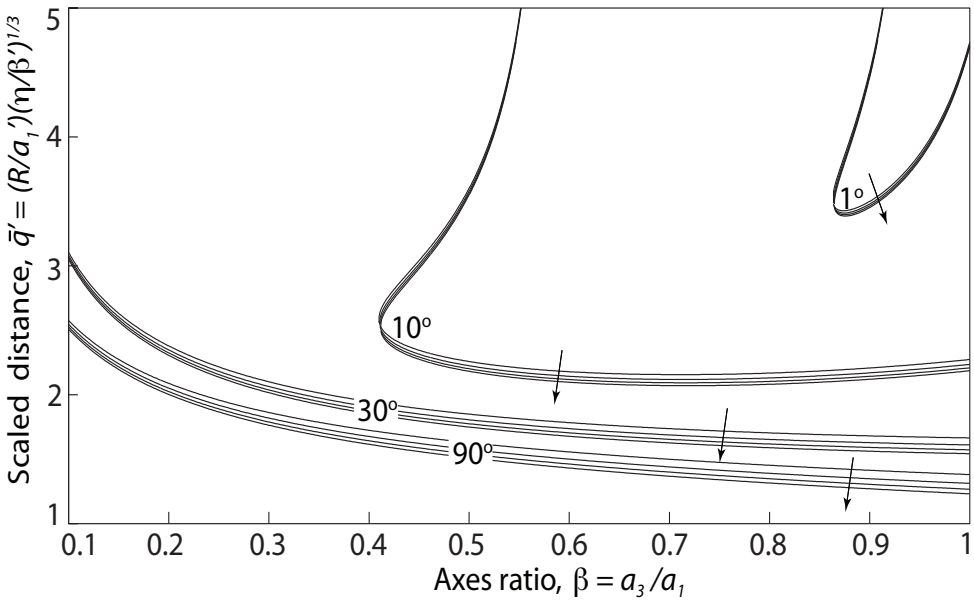


(b) average-triaxial satellites with $\alpha = (1 + \beta)/2$

Fig. 6. Variation of the equilibrium landscape with the primary's oblateness $\beta'$. The equilibrium landscapes are for sections corresponding to prolate and average-triaxial-ellipsoidal satellites. Four values of $\beta'$ are explored: 0.4, 0.6 0.8 and 1. The arrows indicate *increasing* $\beta'$. Several friction angles $\phi_F$ are investigated as indicated.

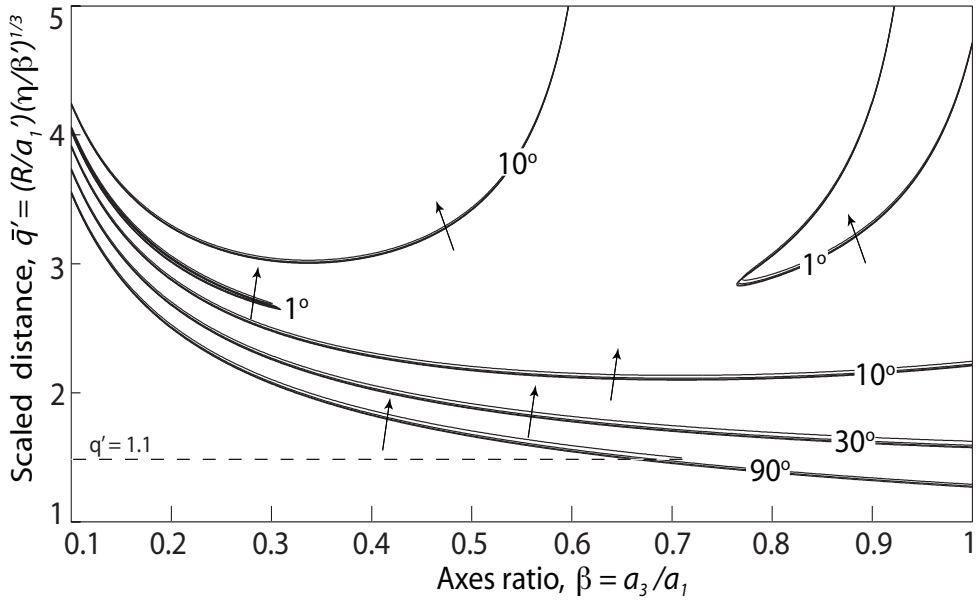


(a) Prolate satellites with $\alpha = \beta$

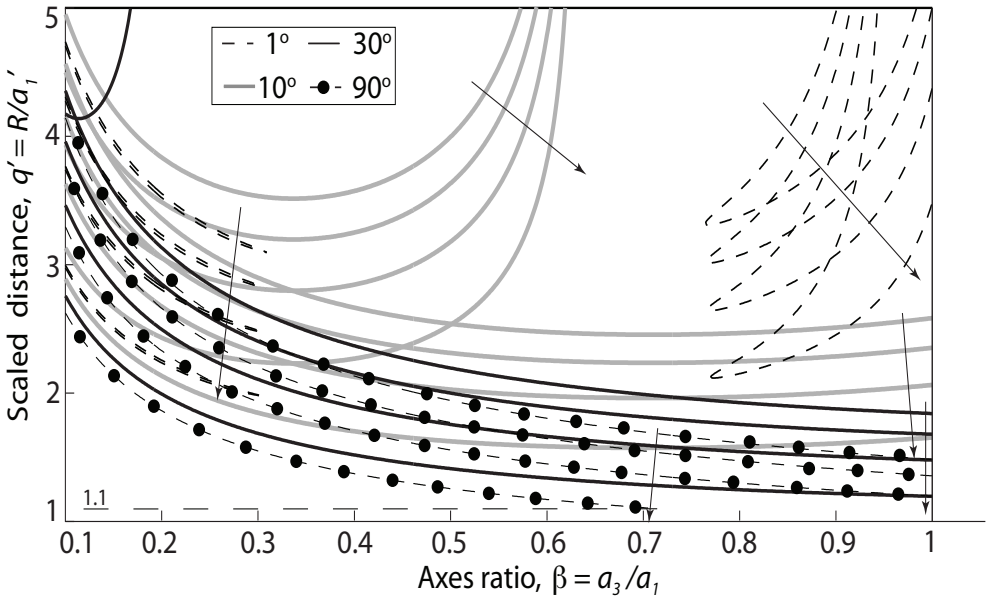


(b) Prolate satellites with $\alpha = \beta$

Fig. 7. Variation of the equilibrium landscape with the density ratio $\eta = \rho/\rho'$. The equilibrium landscape are for sections corresponding to only prolate satellites. Four values of $\eta$ are explored: 0.5, 1, 1.5 and 2. The arrows indicate *increasing* $\eta$. Several friction angles $\phi_F$ are investigated as indicated.

variations. In physical space, because $q' \propto \overline{q}'/\eta^{1/3}$, the equilibrium region for any $\phi_F$ moves further away from the primary as $\eta$ decreases, as is borne out by Fig. 7(b) where we plot the critical curves in $\beta - q'$ space. This behavior is understood easily by recognizing that lower $\eta$ corresponds to greater primary mass, or, correspondingly lower satellite density. While the former circumstance increases the disruptive tidal effect of the primary, the latter reduces the self-gravitational forces that hold the rubble-pile satellite together. Thus, to persist in equilibrium, a granular aggregate has to move further away from a denser primary. Conversely, a denser satellite, with greater self-gravity, can come closer to its primary.

### *4.4 Discussion*

Above, we obtained critical bounds on the equivalent orbital radius $\overline{q}'$ of a tidally-locked rubble-pile ellipsoidal satellite as it moves on a circular path about an oblate primary. Equivalently, the satellite's orbit and internal strength constrained its shape. Employing stresses from (49) in conjunction with the Drucker-Prager yield criterion (37), we generated limits for $\overline{q}'$ as a function of the satellite's internal friction $\phi_F$, its shape $\alpha$ and $\beta$, the primary's oblateness $\beta'$, and the density ratio $\eta$ of the primary to the satellite. We explored this high-dimensional dependency via appropriate two-dimensional planes ($\alpha$-sections) that correspond to self-similar ellipsoidal shapes of the satellite. After fixing $\beta'$ and $\eta$, on any $\alpha$-section, the friction angle $\phi_F$ identifies a region in $\beta - \overline{q}'$ space within which a rubble-pile with at least that much $\phi_F$ may exist in equilibrium. This region, except for $\phi_F = 90^o$, had both lower and upper limits. At $\phi_F = 90^o$, the upper limit moved to infinity. Both these bounds were understood in terms of the interplay between the debilitating tidal and centrifugal stresses and the fortifying self-gravity, and tracing the source of high shear stresses at failure. Analogies were drawn with previous equilibrium analysis for a rubble pile in pure spin (Sharma et al. 2008). We also saw how these equilibrium landscapes help constrain an object's physical and orbital parameters. Finally, the effect of varying the primary's oblateness and changing the density ratio was also noted. Typically, with decreasing $\beta'$ and/or $\eta$, the allowed equilibrium region moves away from the primary. For the same mass, a more flattened planet, i.e., with lower $\beta'$, has greater disruptive tidal influence. Similarly, low-density objects tend to disrupt more easily, as tidal effects then dominate the self-gravity holding the satellite together.

As mentioned in the Introduction, volume-averaging, in the case of cohesionless rubble piles in pure spin (Sharma et al. 2008), precisely matched the exact results of Holsapple (2001) that were in turn based on the method of limit analysis (Chen and Han 1988). Here too, we predict that the constraints on $q'$ obtained above by volume-averaging will be the same as those from limit

analysis. Indeed, this is the case for the Roche problem discussed in Sec. 5. However, caution must be exercised, because as mentioned in Sharma et al. (2008), there is no known fundamental reason for this coincidence between a volume-averaged approach and limit analysis. It is also unclear when and under what conditions will the outcomes of these two methods agree. In fact, if the granular aggregate had a small amount of cohesion, the conclusions of limit analysis and volume-averaging will differ. However, recently Holsapple (2008) has shown that yield predictions predicated on average stresses are an upper bound to the exact results of limit analysis for rigid-plastic materials, i.e., if a rigid-plastic object yields on average, it will definitely yield.

Finally, because no satellite or primary is a perfect ellipsoid, in order profitably to utilize the constraints obtained above, it is necessary to note the effect of surface irregularities. Deviations in the shape of both these bodies from their best-fit ellipsoids will introduce perturbations in the stress field obtained by otherwise approximating these bodies as ellipsoids. If the unevenness is on a scale larger than the constitutive particle size of the granular aggregate, then the perturbation in the stress field will locally violate the yield criterion. Thus, for a rubble-pile satellite modeled as above to survive, it is necessary that the model problem employing nominal [1] ellipsoids for both the satellite and the primary satisfy the conditions for equilibrium obtained above. In other words, for a satellite to exist as a rubble pile with some internal friction angle $\phi_F$, a viable necessary condition is for its associated ellipsoidal shapes to satisfy the bounds associated with an appropriately smoothened primary and that $\phi_F$ (and that ellipsoidal shape).

We now proceed to two applications of the theory developed above. We first specialize to the important case of a spherical primary to recover a generalization appropriate for granular aggregates of the classical Roche problem, and employ it to investigate the two moons of Mars. In the process, we will also make contact with previous work in this area, and also results due to the alternate Mohr-Coulomb yield criterion. Satisfactory results in this simpler case will engender confidence in our more general development, which is then employed to investigate suspected rubble-pile satellites of the giant planets, explicitly accounting for the primary's flattening.

## 5 Application: The Roche problem

In the special case when the primary is a sphere, we recover the classical Roche problem adapted to solid bodies. More precisely, we obtain limits on the orbits that a rubble-pile satellite of a spherical planet may occupy depending on its

[1] Obtained by smoothing irregularities over several particle lengths

internal friction. For a spherical planet, we set $\beta' = 1$ in (45) and (46) and substitute for $B^{(1)}_{111}$ and $B^{(0)}_{33}$ in (49) to obtain the average stresses as

$$\sigma_1 = -\left(A_1 - \frac{2}{\overline{q}'^3}\right)(\alpha\beta)^{-2/3}, \tag{50a}$$

$$\sigma_2 = -\alpha^2 A_2 (\alpha\beta)^{-2/3} \tag{50b}$$

$$\text{and} \quad \sigma_3 = -\beta^2\left(A_3 + \frac{2}{3\overline{q}'^3}\right)(\alpha\beta)^{-2/3}, \tag{50c}$$

where now $\overline{q}' = q'\eta^{1/3}$ is the equivalent distance, and we recall that the expressions for $A_i$ are given in Sec. 2.2. Employing the above stresses with the Drucker-Prager yield criterion as before, we obtain regions in shape ($\beta$) – equivalent distance ($\overline{q}'$) space wherein a tidally-locked rubble-pile satellite of a spherical planet may exist in equilibrium.

Figure 8 displays the results for an oblate satellite, wherein $\alpha = 1$ and $A_1 = A_2$. We see that a fluid oblate satellite cannot exist, and this is consistent with Roche's result (see Chandrasekhar 1969). As the friction angle increases, the region within which a satellite with a given axes ratio $\beta$ may exist as a rubble pile increases. We note that even when consisting of a material with infinite friction, i.e., $\phi_F = 90^o$, an oblate satellite will fail if it gets close enough to the planet. Note that when the friction angle is $90^o$, an object can only fail in tension. This case will be revisited in Sec. 5.2.

At any given axes ratio $\beta$ and friction angle $\phi_F$, there is typically only a lower limit to how close the satellite may come. Exceptions occur over a small $\beta$-range at lower friction angles, e.g., for $0.58 \leqslant \beta \leqslant 0.62$ at $\phi_F = 10^o$. As before, falling below the lower value for $\overline{q}'$ corresponds to yielding due to high shear stresses from increased tidal interaction. Crossing the upper limit, when it exists, indicates an inability of the object to sustain its self-gravitational stresses.

Equilibrium landscapes for other combinations of axes ratios $\alpha$ and $\beta$ may be similarly constructed and explored. We employ one such selection to investigate the moons of Mars next.

### *5.1 Mars*

The red planet Mars is nearly spherical ($\beta' = 0.99$) and has two satellites, Phobos and Deimos. There are suggestions, based on their physical properties such as density, albedo, color and reflectivity that are similar to C-type asteroids, that both these moons are captured asteroids. Burns (1992), however, notes that the calculated histories of orbital evolution of these moons

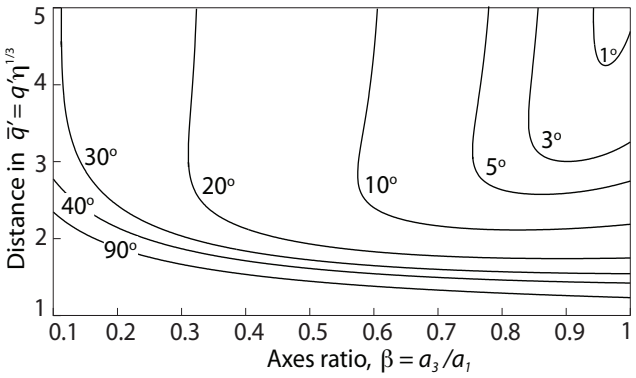


Fig. 8. The equilibrium landscape of a spherical primary's rubble-pile oblate satellite. Curves correspond to various friction angles $\phi_F$, as shown by adjacent numbers.

provides contradictory evidence to the effect that these moons in fact originated in circum-Martian orbit. Nevertheless, for the moment, we will proceed with the assumption that the low density and high porosity of these objects reflects a granular interior. Table 1 lists orbital and physical parameters for these two Martian satellites obtained from NASA's Solar System Dynamics website (http://ssd.jpl.nasa.gov) and Duxbury and Callahan (1989).

Table 1
**Satellites of Mars**. For Mars, $\rho' = 3934$ kg m$^{-3}$ and $\beta' \approx 1$. The satellite's axes ratios $\alpha$ and $\beta$, along with its scaled and equivalent distances from Mars, $q'$ and $\overline{q}'$ respectively, non-dimensional spin rate $W_3$ and orbital period $P$ (in days) are given. $W_3$ is obtained from $q'$ after assuming the satellite to be tidally locked; see Eq. (47).

| *Satellite* | $\alpha$ | $\beta$ | $q'$ | $\eta = \rho/\rho'$ | $\overline{q}' = q'\eta^{1/3}$ | $W_3$ | $P\,(d)$ |
|---|---|---|---|---|---|---|---|
| Phobos | 0.83 | 0.70 | 2.76 | 0.48 | 2.16 | 0.257 | 0.319 |
| Deimos | 0.83 | 0.72 | 6.91 | 0.38 | 4.98 | 0.073 | 1.262 |

Both Phobos and Deimos have roughly the same axes ratio $\alpha$, so we may locate these two Martian satellites on the same $\alpha = 0.83$ $\alpha$-section after setting $\beta' = 1$ for Mars. Figure 9 shows the results in $\beta - \overline{q}'$ space.

We see from Fig. 9 that Deimos lies just outside the $\phi_F = 5^o$ critical curve, while Phobos lies very nearly on the $\phi_F = 10^o$ equilibrium boundary. Thus, both satellites are well within the $\phi_F = 30^o$ equilibrium bounds appropriate for most granular aggregates. However, as Phobos moves closer to Mars at the rate of about 4 meters per century (see, e.g., Shor 1975), in about 2000 years its $\overline{q}'$ will reduce to 1.54. This corresponds to nearly two Martian radii. At this stage, a granular Phobos will cross the $\phi_F = 40^o$ equilibrium curve and may begin to disrupt. It is interesting to note that Dobrovolskis (1982), modeling Phobos as a linear-elastic solid with a yield criterion analogous to the one employed here, predicts a similar critical distance from Mars for Phobos to begin to shed material. We discuss Dobrovolskis' work further in the next section. We also note that the disruption time scale obtained above is a rough

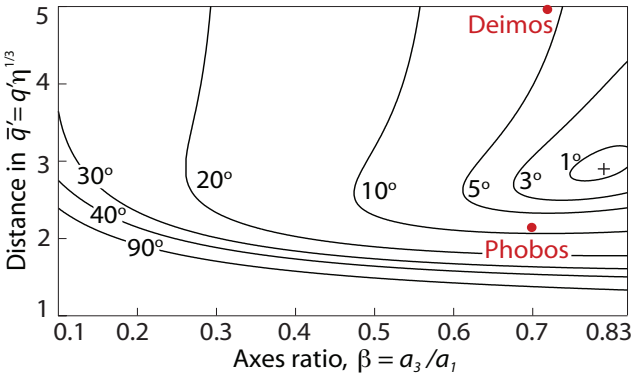


Fig. 9. The two Martians shown on the planar section $\alpha = 0.83$ of the three-dimensional $\alpha - \beta - \bar{q}'$ space. The primary's axes ratio $\beta'$ was set to one. Curves correspond to particular choices of the friction angle $\phi_F$, as indicated by the adjacent numbers. The Darwin ellipsoid associated with $\phi_F = 0^o$ is indicated by a '+' symbol. The upper limit is set by the requirement $\beta \leqslant \alpha$.

estimate; the actual time may well be shorter as Phobos accelerates as it moves closer to Mars. Finally, compared to Phobos, Deimos is much more conveniently placed to survive as a rubble pile.

We next compare the results for the Roche problem with answers due to a different choice of the yield criterion, and also make contact with previous research.

### *5.2 Alternate yield criteria and previous work*

In Sec. 3 we discussed the Mohr-Coulomb failure law as an alternative to the Drucker-Prager yield criterion. Because both these yield criteria are extensively employed in geophysical research (Chen and Han 1988), we provide a quick comparison between their predictions. In Fig. 10 we juxtapose the equilibrium landscape for a tidally-locked prolate rubble pile in orbit about a spherical planet as obtained from both the Mohr-Coulomb and the Drucker-Prager yield criteria. We see that the equilibrium landscape due to the Mohr-Coulomb failure law is contained within that of the Drucker-Prager yield criterion. This feature was also noted for the case of a granular aggregate in pure spin by Sharma et al. (2008). A consequence is that objects that are suspected *not* to be rubble piles when tested with a Mohr-Coulomb criterion, may be perfectly acceptable when examined as Drucker-Prager materials. As mentioned earlier, Sharma et al. (2006) have noted that numerical simulations suggest that the Drucker-Prager yield criterion may be better suited for granular aggregates. Hence, we preferred the Drucker-Prager criterion in this work.

The Mohr-Coulomb yield criterion provides an important point of contact with the earlier work of Davidsson (2001). He found the Roche limit for solid

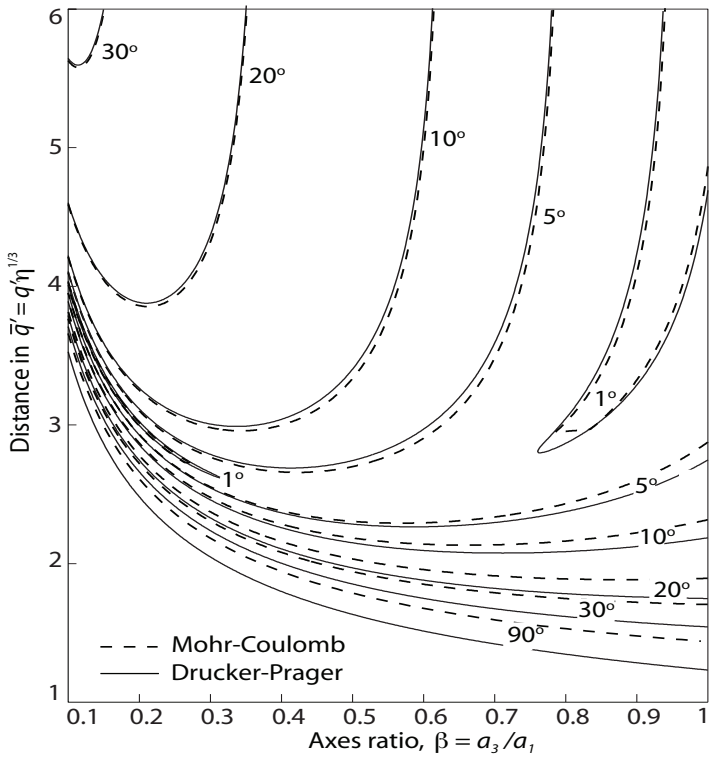


Fig. 10. The equilibrium landscape of a prolate satellite due to applications of the Mohr-Coulomb and Drucker-Prager yield criteria. Curves are drawn for various friction angles as shown.

axi-symmetric objects in orbit about a spherical primary by assuming first a failure plane within the satellite. Parts of the object on either side of this failure plane were treated as separate entities that interact across this plane. Stresses were calculated by dividing the net interaction force by the plane's area. Davidsson (2001) assumed that the object failed when the stress normal to the failure plane surpassed the constituent material's tensile strength. Amongst all possible planes, the critical failure plane was that plane across which the interaction stress first became zero. This method of stress analysis is reminiscent of basic engineering mechanics, and is often useful for obtaining first estimates. It neglects local variations of stress, and instead works with stress averages over larger cross-sections. In the case of prolate ellipsoids, Davidsson (2001) found the critical failure plane to be the symmetry plane perpendicular to the long axis that itself points towards the primary. Assuming that the satellite has no tensile strength, Davdisson's (2001) results may be put into the following form:

$$\overline{q}'_D = \left(\frac{4\pi}{\varepsilon}\right)^{1/3},$$

where $\overline{q}'_D$ is the *closest* a satellite may to a planet before failing, and

$$\varepsilon = \frac{4\pi f}{(f^2-1)^{3/2}} \ln\left(f + \sqrt{f^2-1}\right) - \frac{4\pi}{f^2-1},$$

with $f = 1/\beta$. Thus, the above generates the equilibrium curve $\overline{q}'_D(\beta)$, and all objects that have $\overline{q}' \geqslant \overline{q}'_D$ will, according to Davidsson (2001), exist in equilibrium. For comparison, in Fig. 11 we plot Davidsson's (2001) results along with ours for a material with $\phi_F = 90^o$ employing both the Mohr-Coulomb and the Drucker-Prager yield criteria. It is seen that Davidsson's (2001) results exactly match ours for a Mohr-Coulomb material with an internal friction angle of $\phi_F = 90^o$. Recall that $\phi_F = 90^o$ corresponds to infinite frictional resistance, i.e., the body can support any amount of shear stress and will fail only when any one of the principal averaged stresses first becomes tensile. This match thus offers a more rigorous support of Davidsson's (2001) results: Davidsson's (2001) analysis precisely corresponds to seeking yielding of a Mohr-Coulomb material with infinite shear resistance in a volume-averaged sense. Recalling that volume-averaging gives *exactly* the same results as limit analysis for a cohesion-less material puts the work of Davidsson (2001) on a very firm foundation. It should be noted that coincidence with Davidsson (2001) is, however, not reason enough to prefer one yield criterion over the other when investigating granular aggregates. We are interested in employing the yield criterion that is best suited for rubble-piles, and as we saw above, Davidsson's (2001) analysis is applicable only to solid bodies with no tensile strength.

In the context of Davidsson's (2001) work, it is important to mention that several other researchers have investigated the Roche limit for coherent solid bodies. These include Aggarwal and Oberbeck (1974) and Dobrovolskis (1982, 1990). In these, the stresses within the satellite were derived after modeling the satellite as a *linear-elastic* body. Aggarwal and Oberbeck (1974) assumed an isotropic, incompressible, homogeneous and spherical satellite. Dobrovolskis (1982) introduced a novel procedure to analyze the linear-elastic response of triaxial objects, and applied his results to investigate the internal stresses of Phobos; see also Sec. 5.1. Retaining the satellite's triaxiality, Dobrovolskis (1990) extended his previous calculation to also allow for compressibility, but ultimately specialized his results to a spherical satellite. A thorough overview and comparison is available in Davidsson (1999). We remind the reader that the present work focuses on rubble-piles, so that a linear-elastic analysis will not be appropriate. Only in the limit of infinite internal friction (perfect interlocking), the case considered above, does a rubble pile respond like – in the sense of the above-cited works – a coherent solid object with zero tensile strength. We note that Dobrovolskis (1982, 1990) himself acknowledges the different behavior of granular geophysical materials when he introduces for them a general criterion due to Navier (Dobrovolskis 1982, p. 143, Eq. 28; Dobrovolskis 1990, p. 28, Eq. 6), similar in form to the Mohr-Coulomb criterion.

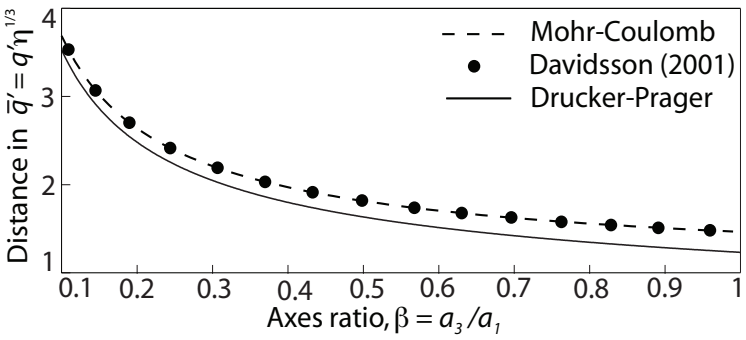


Fig. 11. Equilibrium curve for a prolate satellite due to Davidsson (2001), compared with those due to the Mohr-Coulomb and Drucker-Prager criteria at a friction angle $\phi_F = 90^o$.

However, the stresses he employs are still obtained from a linear-elastic analysis. In passing, we note that it is possible, within the present volume-averaging framework, to consider a linear-elastic satellite, thereby making explicit contact with the results of Aggarwal and Oberbeck (1974) and Dobrovolskis (1982, 1990).

A Roche limit suitable for rubble piles was first obtained by Sharma et al. (2005a) to investigate the possible granular nature of Jupiter's satellite Amalthea. Sharma et al. (2006) further used this Roche limit to explain results obtained from their own tidal disruption calculations. To this end, dynamical effects of tidal torques due to misaligned satellites were retained. Recall, that the tidal torques and the accompanying angular acceleration vanish whenever the satellite's principal axis points towards the primary. Burns et al. (2007) provided a unified treatment to both these dynamical aspects of the Roche problem. Later, Holsapple and Michel (2006, 2008) extensively studied the Roche problem for solid satellites about spherical primaries. They employed a static version of Signorini's theory of stress means (Truesdell and Toupin 1960, p. 574) that at the *lowest* order of approximation, in *statics* coincides with the approach employed here. Consequently, for the Roche problem our results and those of Holsapple and Michel (2006, 2008) match. A more detailed comparison between the two techniques is given by Sharma et al. (2008). Holsapple and Michel (2006, 2008) investigated several possible tidally-locked orientations of the satellite with respect to the primary. Internal cohesion was also considered. However, because the satellite was always aligned with a symmetry axis pointing to the primary, tidal torques played no role. Theirs was a static calculation. In fact, except for Sharma et al. (2006), all calculations neglect the effect of tidal torques and angular acceleration on the Roche limit, preferring to align the satellite suitably so as to negate tidal torques. A satellite's rotation rate is, however, seldom constant, changing as a result of tidal torques, elliptic and/or inclined orbits, etc.; an analysis of the consequences of this misalignment may well be meaningful. This may accomplished in a straightforward manner by a dynamical version of the present calculation.

## 6 Application: The giant planets

The inner satellites of the giant planets Neptune, Uranus, Saturn and Jupiter are widely suspected to have rubble interiors both due to their relatively low densities, and their suspected accretionary origins; see, e.g., Burns et al. (2004), Porco et al. (2006), or Banfield and Murray (1992). Tables 2 - 5 list relevant data for these satellites. Employing the equilibrium landscape of Sec. 4 for rubble-pile satellites of oblate primaries, we now proceed to test whether these objects can exist as granular aggregates held together by self-gravity alone.

In Sec. 4, we saw that the equilibrium of a tidally-locked rubble-pile satellite is governed by its shape ($\alpha$ and $\beta$), the planet's oblateness $\beta'$, the distance $q'$ between them and the density ratio $\eta = \rho/\rho'$. Thus, even within the same planetary satellite system, because the ratio $\eta$ may be different, several plots will be required. This may be avoided by retaining only the first term in the expansion given in (45) and (46) for the coefficients $B_{ij}^{(0)}$ and $B_{ijk}^{(1)}$, and then absorbing both $\eta$ and $\beta'$ into $q'$ to define the equivalent distance $\overline{q}' = q'(\eta/\beta')^{1/3}$. The error introduced by this truncation will be of the order of $(1-\beta'^2)/q'^2$, a small quantity; this is about 4% for Pan, Saturn's innermost satellite. Indeed, with this approximation we find the stresses from (49) to be

$$\sigma_1 = -\left(A_1 - \frac{2}{\overline{q}'^3}\right)(\alpha\beta)^{-2/3}, \tag{51a}$$

$$\sigma_2 = -\alpha^2 A_2 (\alpha\beta)^{-2/3} \tag{51b}$$

$$\text{and} \quad \sigma_3 = -\beta^2\left(A_3 + \frac{2}{3\overline{q}'^3}\right)(\alpha\beta)^{-2/3}, \tag{51c}$$

where, again, the $A_i$ depend on the satellite's shape (see Sec. 2.2), and the stresses must not violate the yield criterion (37). Because both $\beta'$ and $\eta$ are absent from the above equations, the equilibrium landscape of all tidally-locked satellites may be analyzed on the basis of only their shape ($\alpha$ and $\beta$), and their equivalent distance $\overline{q}' = q'(\eta/\beta')^{(1/3)}$.

### *6.1 Satellite data*

*Neptune*

Of Neptune's thirteen satellites, the six inner ones, Naiad, Thalassa, Despina, Galatea, Larissa and Proteus are believed to have accreted from the debris resulting from Triton's capture by Neptune (Banfield and Murray 1992). Except for Galatea, whose density was estimated by Porco (1991) to be a

low 750 kg $m^{-3}$, little is known about the density of the remaining satellites. We shall assume their densities to be 1200 kg $m^{-3}$ – the average of Galatea's and Neptune's densities. The shapes of these satellites were taken from Karkoschka (2003), while their orbital specifications are from Jacobson and Owen (2004). Because of large errors in computing the satellite's semimajor axes (see Karkoschka 2003, Table 1), the axes ratios $\alpha$ and $\beta$ are computed only to the first decimal place in Table 2. Neptune itself is an oblate body with density of 1600 kg $m^{-3}$ and axes ratio $\beta' = a_3'/a_1' = 0.98$.

Table 2
**Satellites of Neptune**. For Neptune, $\rho' = 1600$ kg $m^{-3}$ and $\beta' = 0.98$. Data for the six innermost moons are displayed. See also Table 1's caption.

| *Satellite* | $\alpha$ | $\beta$ | $q'$ | $\eta = \rho/\rho'$ | $\overline{q}' = q'\,(\eta/\beta')^{1/3}$ | $W_3$ | $P\,(d)$ |
|---|---|---|---|---|---|---|---|
| Naiad | 0.6 | 0.5 | 1.95 | 0.73 | 1.95 | 0.348 | 0.294 |
| Thalassa | 0.9 | 0.5 | 2.02 | 0.73 | 1.83 | 0.329 | 0.311 |
| Despina | 0.8 | 0.7 | 2.12 | 0.73 | 1.92 | 0.307 | 0.335 |
| Galatea | 0.9 | 0.7 | 2.50 | 0.46 | 1.94 | 0.303 | 0.429 |
| Larissa | 0.9 | 0.8 | 2.97 | 0.73 | 2.69 | 0.185 | 0.555 |
| Proteus | 0.9 | 0.9 | 4.75 | 0.73 | 4.31 | 0.091 | 1.122 |

*Uranus*

Uranus' satellites number 23. Of these, we consider the possibility of the thirteen small inner moons to be rubble piles. This is in concordance with the observation of Thomas et al. (1989) that the compositions of these small satellites are similar to those of neighboring ring particles, suggesting an accretionary origin. Data for these are displayed in Table 3. Karkoschka (2001) provides information for the shapes of all except Cupid and Mab. However, only $a_2/a_1$ is reported, and we assume that $\beta = a_3/a_1 = a_2/a_1 = \alpha$, i.e., these objects are proloidal in shape. For Cupid and Mab, Showalter and Lissauer (2006) estimate their mean radii to be 9 and 12 km, respectively, and also update Perdita's size to 13 km. Showalter and Lissauer (2006) provide orbital data for Cupid, Perdita and Mab, while Jacobson (1998) furnishes $q'$ for the remaining moons. As in the case of Neptunian satellites, there are large errors in the satellite's computed shape, and this uncertainty (from Karkoschka 2001, Table V) is noted for most moons in Table 3 explicitly. There are no available estimates for the densities of these objects, and we take their densities to be equal to that of Uranus' 1270 kg $m^{-3}$.

*Saturn*

Saturn has 60 named moons. Of these, we select the fourteen small inner satellites listed in Table 4 as candidate rubble piles. The satellites are arranged

Table 3
**Satellites of Uranus**. For Uranus, $\rho' = 1270\text{kg m}^{-3}$ and $\beta' = 0.977$. Data for the inner thirteen satellites are displayed. We assume all satellites to have $\alpha = \beta$ and $\rho = \rho'$, so that $\eta = 1$ and $\overline{q}' = q'/\beta'^{1/3}$. See also Table 1's caption.

| *Satellite* | $\alpha = \beta$ | $q'$ | $\overline{q}' = q'/\beta'^{1/3}$ | $W_3$ | $P\,(d)$ |
|---|---|---|---|---|---|
| Cordelia | $0.7 \pm 0.2$ | 1.95 | 1.97 | 0.298 | 0.335 |
| Ophelia | $0.7 \pm 0.3$ | 2.10 | 2.12 | 0.265 | 0.376 |
| Bianca | $0.7 \pm 0.2$ | 2.31 | 2.33 | 0.229 | 0.435 |
| Cressida | $0.8 \pm 0.3$ | 2.42 | 2.44 | 0.215 | 0.464 |
| Desdemona | $0.6 \pm 0.2$ | 2.45 | 2.47 | 0.211 | 0.474 |
| Juliet | $0.5 \pm 0.1$ | 2.52 | 2.54 | 0.202 | 0.493 |
| Portia | $0.8 \pm 0.1$ | 2.59 | 2.61 | 0.194 | 0.513 |
| Rosalind | $1 > 0.8$ | 2.74 | 2.76 | 0.179 | 0.558 |
| Cupid | 1 | 2.91 | 2.93 | 0.163 | 0.618 |
| Belinda | $0.5 \pm 0.1$ | 2.94 | 2.96 | 0.160 | 0.624 |
| Perdita | 1 | 2.99 | 3.01 | 0.156 | 0.638 |
| Puck | $1 > 0.93$ | 3.36 | 3.39 | 0.131 | 0.762 |
| Mab | 1 | 3.82 | 3.85 | 0.108 | 0.923 |

in order of increasing distance $q'$ from Saturn. Possible accretionary origins of these satellites has been explored earlier by Porco et al. (2007). Here we revisit this possibility in light of the equilibrium theory developed above for rubble-pile satellites. The best-fit ellipsoidal shapes of all except Janus, Epimetheus, Anthe and Methone have been provided by Porco et al. (2007). For Janus and Epimetheus, we take the semi-major axes to be 100, 95 and 76 kms., and 63, 55 and 51 kms., respectively [2] . Anthe and Methone are assumed to be spherical with mean radii of 1.8 km (Cooper et al. 2008) and 3 km (Porco et al. 2005), respectively. Densities of only Pan, Atlas, Prometheus, Pandora, Janus and Epimetheus have been estimated using their $Gm$ values provided by Jacobson et al. (2008). For the remaining objects we assign arbitrarily a density of 1000 kg m$^{-3}$. The orbital data of Telesto, Calypso and Helene is given by Porco et al. (2007), for Anthe by Cooper et al. (2008), and for the remaining satellites by Jacobson et al. (2008).

### *6.1.1 Jupiter*

Only the four inner moons of the bountiful 63 satellites of Jupiter are suspected accreted granular aggregates on nearly equatorial orbits. In the past, Richardson et al. (2005) have explored Amalthea's rubble-pile nature by a $n$-body code. The relevant data for these four objects are given in Table 5. The satellites' shapes are taken from Thomas et al. (1998). The orbital data for Amalthea and Thebe are from the recent work of Cooper et al. (2006), while those for Metis and Adrastea have been given earlier by Burns et al. (2004). The density of only Amalthea has been estimated at a low $857 \pm 99$ kg m$^{-3}$

[2] P. C. Thomas, private communication

Table 4
**Satellites of Saturn**. For Saturn, $\rho' = 690$ kg m$^{-3}$ and $\beta' = 0.902$. Data for the fourteen inner satellites are displayed. See also Table 1's caption.

| *Satellite* | $\alpha$ | $\beta$ | $q'$ | $\eta = \rho/\rho'$ | $\overline{q}' = q' \left(\eta/\beta'\right)^{1/3}$ | $W_3$ | $P\,(d)$ |
|---|---|---|---|---|---|---|---|
| Pan | 0.9 | 0.6 | 2.22 | 0.6 | 1.93 | 0.306 | 0.575 |
| Daphnis | 1 | 0.7 | 2.26 | 0.5 | 1.85 | 0.325 | 0.594 |
| Atlas | 0.9 | 0.4 | 2.28 | 0.67 | 2.07 | 0.276 | 0.602 |
| Prometheus | 0.6 | 0.5 | 2.31 | 0.68 | 2.11 | 0.268 | 0.613 |
| Pandora | 0.8 | 0.6 | 2.35 | 0.73 | 2.19 | 0.253 | 0.629 |
| Epimetheus | 0.9 | 0.8 | 2.51 | 1.00 | 2.6 | 0.195 | 0.694 |
| Janus | 1 | 0.8 | 2.51 | 0.92 | 2.52 | 0.204 | 0.695 |
| Methone | 1 | 1 | 3.22 | 1.45 | 3.77 | 0.111 | 1.010 |
| Anthe | 1 | 1 | 3.28 | 1.45 | 3.84 | 0.109 | 1.037 |
| Pallene | 0.8 | 0.7 | 3.52 | 1.45 | 4.12 | 0.097 | 1.154 |
| Telesto | 0.7 | 0.7 | 4.89 | 1.45 | 5.73 | 0.060 | 1.888 |
| Calypso | 0.8 | 0.4 | 4.89 | 1.45 | 5.73 | 0.060 | 1.888 |
| Polydeuces | 0.8 | 0.7 | 6.26 | 2.17 | 8.39 | 0.034 | 2.737 |
| Helene | 1 | 0.6 | 6.26 | 1.45 | 7.33 | 0.041 | 2.737 |

by Anderson et al. (2005). For the three remaining satellites, we arbitrarily assign a density of 860 kg m$^{-3}$ to match Amalthea's.

Table 5
**Satellites of Jupiter**. For Jupiter, $\rho' = 1300$ kg m$^{-3}$ and $\beta' = 0.935$. Data for the four inner moons are displayed. See also Table 1's caption.

| *Satellite* | $\alpha$ | $\beta$ | $q'$ | $\eta = \rho/\rho'$ | $\overline{q}' = q' \left(\eta/\beta'\right)^{1/3}$ | $W_3$ | $P\,(d)$ |
|---|---|---|---|---|---|---|---|
| Metis | 0.7 | 0.6 | 1.79 | 0.65 | 1.59 | 0.412 | 0.295 |
| Adrastea | 0.8 | 0.7 | 1.80 | 0.65 | 1.59 | 0.407 | 0.298 |
| Amalthea | 0.6 | 0.5 | 2.54 | 0.65 | 2.24 | 0.244 | 0.498 |
| Thebe | 0.8 | 0.7 | 3.10 | 0.65 | 2.75 | 0.180 | 0.675 |

### *6.2 Locations*

We explore the existence of the above satellites as possible rubble piles by locating them on appropriate $\alpha$-sections (see Sec. 4) of the three-dimensional shape–distance $\alpha - \beta - \overline{q}'$ equilibrium region. Because not all the above moons are self-similar, several such $\alpha$-sections will be required. In particular, the planar sections, $\alpha = 1$, $\alpha = 0.9$, $\alpha = 0.8$, $\alpha = 0.7$, $\alpha = 0.6$ and $\alpha = \beta$ are found sufficient. This is accomplished in Figs. 12(a) - 14 that we discuss in the next section. The satellites of Neptune, Saturn and Jupiter are dealt with simultaneously, while Uranus' prolate moons are collected on a separate plot.

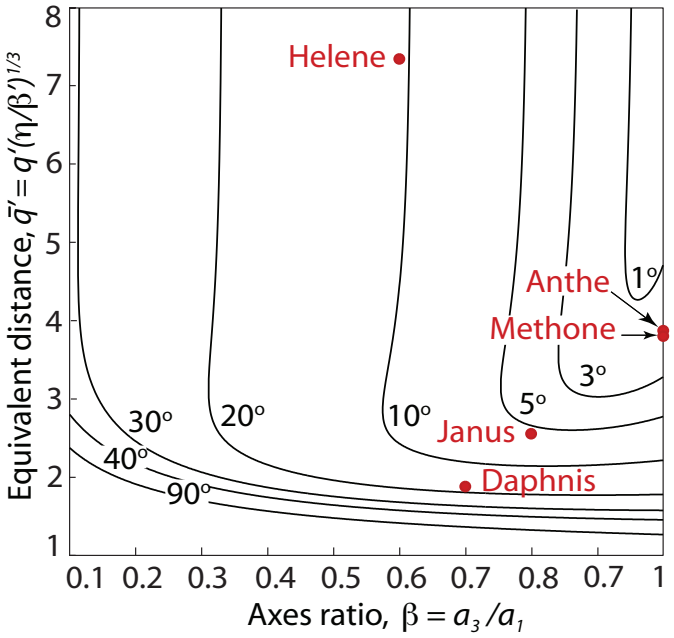


(a) $\alpha = 1$.

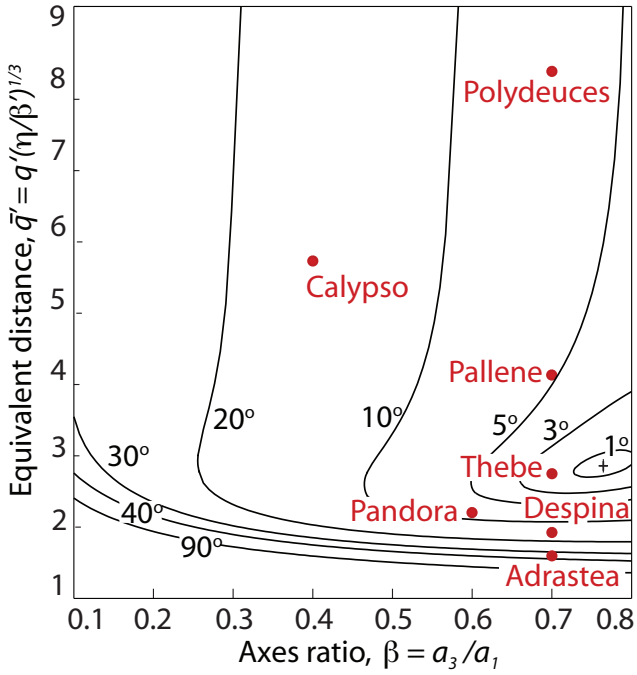


(b) $\alpha = 0.8$.

Fig. 12. The inner moons of Neptune, Saturn and Jupiter shown on planar sections of the three-dimensional $\alpha - \beta - \overline{q}'$ space obtained by suitable specifications of $\alpha$. Curves correspond to particular choices of the friction angle $\phi_F$, as indicated by the adjacent numbers. Where it exists, the Darwin ellipsoid associated with $\phi_F = 0^o$ is indicated by a '+' symbol. In both figures, the abscissa's upper limit is set by the requirement $\beta \leqslant \alpha$.

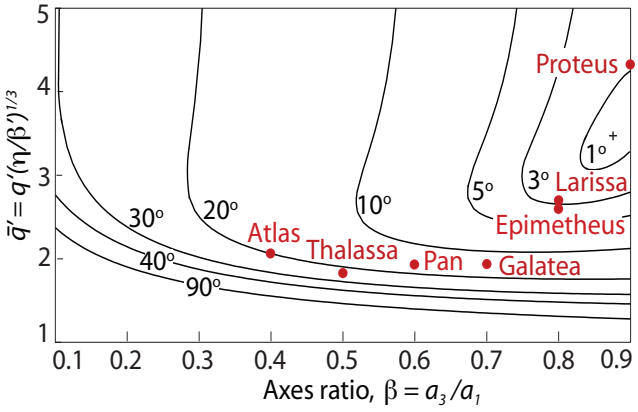


(a) $\alpha = 0.9$.

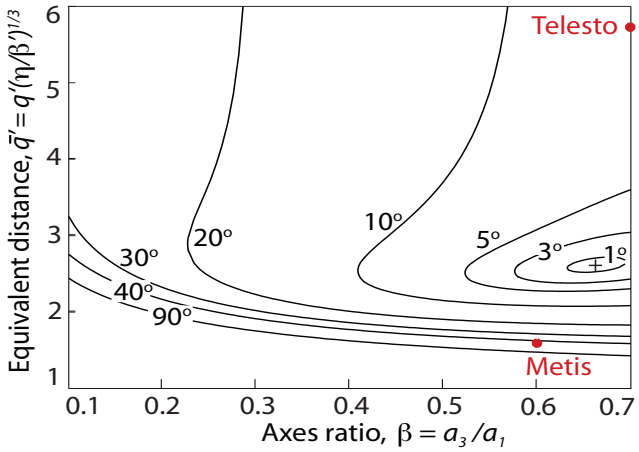


(b) $\alpha = 0.7$.

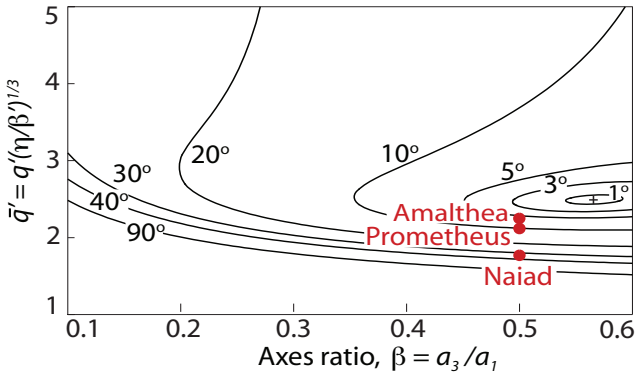


(c) $\alpha = 0.6$.

Fig. 13. The plot of the inner moons of Neptune, Saturn and Jupiter continued from Fig. 12. See also Fig. 12's caption.

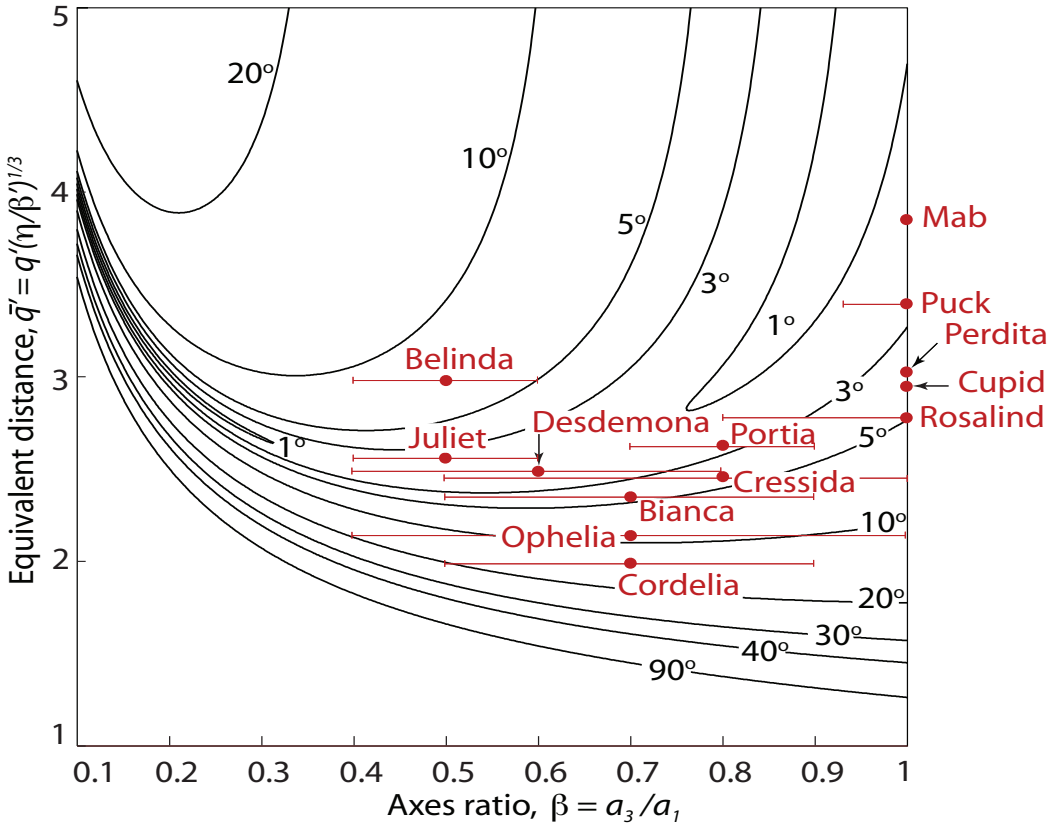


Fig. 14. The thirteen small inner moons of Uranus shown on the $\alpha$-section $\alpha = \beta$ of the three-dimensional $\alpha - \beta - \overline{q}'$ space. The error bars depict the uncertainty in the axes ratio listed in Table 3. Curves correspond to particular choices of the friction angle $\phi_F$, as indicated by the adjacent numbers.

### *6.3 Discussion*

*Neptune*

We see from Figs. 13(a) and 12(b) that Galatea, Larissa, Proteus and Despina, all lie within the $\phi_F = 20^o$ curves. This means that they require an internal friction of at most $20^o$. Of course, the friction can be higher, as the equilibrium curves provide only a necessary requirement on internal strength. Nevertheless, these bodies appear not to violate the constraint $\phi_F \approx 30^o$ true for most granular aggregates like soils (see, e.g., Nedderman 1992). Proteus, strikingly, appears to have relaxed to a shape appropriate for a fluid object, as indicated by its proximity to the Darwin ellipsoid in Fig. 13(a). From the same figure, we observe that Thalassa resides between the $\phi_F = 20^o$ and $\phi_F = 30^o$ curves, which also is supportive of a rubble-pile hypothesis.

The moon Naiad, in Fig. 13(c), lies outside the $\phi_F = 30^o$ equilibrium curve. Thus, if indeed Naiad is a rubble pile, it may be dangerously close to dis-

ruption. Orbital perturbations that bring Naiad closer to Neptune may well cause the satellite to lose material. At the same time, a friction angle greater than $30^o$ may be too high for a rubble-pile given Naiad's assumed density of 1200 kg $m^{-3}$. This is because the internal frictional resistance of granular aggregates is due both to particle inter-locking and to their superficial sliding. The former *geometric* source of friction is typically dominant, but decreases with lowering density. Thus, if Naiad's actual density was any lower, say equal to water's, the resulting smaller $\overline{q}' = 1.66$ would push Naiad beyond the $\phi_F = 40^o$ curve, making Naiad's existence as a rubble pile highly suspect. Several other possibilities also suggest themselves. An obvious resolution is that Naiad's density is higher; a density equal to Neptune's 1600 kg $m^{-3}$ raises Naiad's $\overline{q}'$ to 1.96 from its present value of 1.77, putting it comfortably within the $\phi_F = 20^o$ equilibrium region. However, too high a density may cast doubt over Naiad's genesis by an accumulation of ring/debris particles. Another likelihood is that Naiad to some degree is a coherent structure. This structure may be a reflection of welding that might have taken place between Naiad's assembled constituents due to gravitational pressure. Coherence could also be a signature of the fact that Naiad may not even be a rubble pile, but a cellular honeycomb-like structure with large micro-porosity but also some tensile strength. Of course, the latter interpretation would again be contrary to Naiad's suspected accretionary origins. Inter-particle cohesion is another factor that helps an object sustain higher shear stresses. However, because cohesion depends on particle size and their packing density, it may not be significant at planetary sizes and/or a density of 1200 kg $m^{-3}$.

*Uranus*

Here, because the satellites' shapes are all assumed proloidal or spherical, we require only the planar section $\alpha = \beta$ to represent them together. This is done in Fig. 14, where we also show the uncertainty in the satellite's shape. We see that except for Cordelia, Ophelia and Belinda, all other moons require a maximum internal friction of $5^o$ to survive as rubble piles. Amongst the rather elongated moons Belinda, Juliet and Desdemona, the latter two are positioned rather delicately within the narrow portion of the $\phi_F = 3^o$ equilibrium region. Interestingly, even after Juliet's uncertainty in shape is accounted for, it still remains within the $\phi_F = 3^o$ limits. This seems to suggest that Desdemona, and more so Juliet, may possibly have low resistance to shear stresses. Bianca, Cressida and Rosalind cluster near the lower $\phi_F = 5^o$ stability curve. Thus, if we assume that these objects too were unable to support any significant shear stress, they may tidally disintegrate if they moved any closer to Uranus. Ophelia lies close to the lower $\phi_F = 10^o$ curve, while Cordelia is below that curve, revealing that these two objects may well have some internal friction. Note that the left end of the error bar takes both Ophelia and Cressida close to the lower $\phi_F = 20^o$ bound. Cigar-like Belinda lies between the $\phi_F = 5^o$

and $\phi_F = 10^o$ curves. Spread in its location due shape uncertainties still keep it within this region. Finally, if Belinda's density were about 1900 kg $m^{-3}$ rather than the assumed 1270 kg $m^{-3}$, Belinda would require enough frictional strength to prevent gravitational collapse. Recall that crossing the upper bounding curve represents inability of the body to sustain its internal gravity. For a more careful analysis of Uranus' moons, much more information about their shapes and densities would be required.

*Saturn*

From Figs. 12 and 13 we observe that all of Saturn's inner moons fall within the equilibrium curves corresponding to a friction angle of $20^o$. This is encouraging, as it supports the hypothesis that these low-density objects formed through an accretion of ring particles around an initial seed mass (Porco et al. 2007). Atlas, Pan and Daphnis appear to be the only satellites that have utilized their increased internal shear resistance to explore equilibrium regions accessible to rubble piles. In fact, other than Atlas, Pan, Calypso and Daphnis, the remaining ten moons all lie inside the $\phi_F = 10^o$ curve. This lack of spread could suggest weak internal friction in Saturn's moons correlated, perhaps, to their low densities; cf. our discussion on Naiad above.

It is instructive to note that if we neglected Saturn's oblateness, Prometheus in Fig. 13(c), in keeping with behavior noted in Fig. 6, would lie well outside the $\phi_F = 10^o$ curve. Similarly, Atlas in Fig. 13(a) would be outside the $\phi_F = 20^o$ equilibrium region, not within.

*Jupiter*

Thebe in Fig. 12(b) lies within the $\phi_F = 3^o$ equilibrium curve, very close to the shape achieved by a fluid ellipsoid at equilibrium, though this does not necessarily imply that Thebe's interior is fluid-like in nature. Amalthea, with a calculated density of 857 kg $m^{-3}$, is shown in Fig. 13(c) to require material with an internal friction angle slightly more than $5^o$ to support itself. This contributes to the hypothesis that this low-density satellite of Jupiter may in fact be a granular aggregate. In fact, at Amalthea's low density, we do note expect it to satisfy high frictional requirements.

Fig. 12(b) shows Adrastea to fall between the $\phi_F = 30^o$ and $\phi_F = 40^o$ equilibrium limits. This is very similar to the Neptunian Naiad in Fig. 13(c), except that Adrastea's assumed density is much lower than Naiad's. Because the equilibrium curves for the higher friction angles bunch up at higher axes ratios $\beta$, slight errors in the satellite's density can drastically influence internal structure hypotheses. Thus, if we allowed for an error of about $\pm 10\%$ in Adrastea's assumed density, we would obtain either 900 kg $m^{-3}$ or 750 kg $m^{-3}$

as its density. The former density would yield a $\overline{q}' \approx 1.64$, locating Adrastea on the $\phi_F = 30^o$ equilibrium curve, thereby lending some support to any proposed rubble-pile model. However, $30^o$ may yet be too high a friction angle notwithstanding Adrastea's suggested higher density of 900 kg m$^{-3}$, and this indicates that Adrastea's density is even greater. In contrast, the lower density of 750 kg m$^{-3}$ is equivalent to a $\overline{q}'$ of about 1.53 which pushes Adrastea outside the $\phi_F = 40^o$ curve, and thereby makes Adrastea's existence as an incoherent, cohesion-less rubble pile extremely uncertain. Similar analyses may be performed for errors in a satellite's orbital radius $q'$, though these tend to be much better constrained.

In Fig. 13(b), Metis lies beyond even the $\phi_F = 40^o$ curve. Recalling that granular aggregates, especially ones with Metis' low density, seldom have friction angles beyond $40^o$, this strongly suggests that Metis' density is in fact higher than its neighbors; recall that $\overline{q}' \sim \rho^{1/3}$. This would be in keeping with the predictions of Thomas et al. (1998), who based on a study of craters on Metis suggested $\rho = 1500$ kg m$^{-3}$. At this density, Metis' $\overline{q}'$ equals 1.92, placing it well within the $\phi_F = 20^o$ curve, a far more appropriate location for a granular Metis. There may also be present some degree of coherence and/or cellular structure and/or inter-particle cohesion; cf., our discussion for Naiad above. Either this, or Metis is on the verge of failure.

## 7 Conclusions

In this paper, we have obtained general equations governing the equilibrium of an ellipsoidal tidally-locked rubble-pile satellite of an ellipsoidal primary. This constituted an extension of the first Darwin problem to the case of granular aggregates. The general formulation was then specialized to the case of ellipsoidal satellites of oblate primaries to investigate the equilibrium of the small inner moons of the giant planets. In addition, we derived a Roche limit suitable for rubble piles in orbit about spherical primaries, and applied it to Mars' moons. We also made contact with the earlier results of Davidsson (2001), and were able to provide a more rigorous rationale for their correctness.

Several immediate avenues of exploration are now available. The first, more straightforward one, is to apply the results in this paper to asteroidal satellites. The second, more involved problem is to investigate the equilibrium of binaries, i.e., systems where both the primary and the satellite are gravitational held granular aggregates of comparable mass. It will also be interesting to explore the dynamical passage into equilibrium of such rubble-pile satellites. As in the case of rubble piles in pure spin, this exercise, apart from providing insight into the accretionary process that formed/shape them, is helpful for comparisons with (as yet unavailable) $n$-body simulations of these granular systems.

## 8 Acknowledgements

I thank Sivasambu Mahesh of Indian Institute of Technology Kanpur, Anindya Chatterjee of Indian Institute of Science, Bangalore, and Joe Burns and Jim Jenkins of Theoretical and Applied Mechanics, Cornell University for helpful discussions. I also thank Anthony Dobrovolskis of Lick Observatory, U. C. Santa Cruz and Dan Scheeres of Colorado University for insightful reviews that have made this work better.

## References

Abramowitz, M., and I. A. Stegun 1965. *Handbook of Mathematical Functions.* New York: Dover.

Aggarwal, H. R., and V. R. Oberbeck 1974. Roche limit of a solid body. *Astrophys. J.* **191**, 577–588.

Anderson, J. D., and 11 others 2005. Amalthea's density is less than that of water. *Science* **308**, 1291–1293.

Ashenberg, J. 2005. Proposed method for modeling the gravitational interaction between finite bodies. *J. Guid. Control Dynam.* **28**, 768–774.

Banfield, D., and N. Murray 1992. A dynamical history of the inner Neptunian satellites. *Icarus* **99**, 390–401.

Belytschko, T., W. L. Liu, and B. Moran 2000. *Nonlinear Finite Elements for Continua and Structures.* NY: John Wiley and Sons.

Burns, J. A. 1992. Contradictory clues as to the origin of the Martian moons. In H. H. Kieffer, B. M. Jakosky, C. W. Snyder, and M. S. Matthews (Eds.), *Mars*, pp. 1283–1301. Tucson, AZ: U. Arizona Press.

Burns, J. A., I. Sharma, and J. T. Jenkins 2007. Approximate equilibrium shapes for spinning, gravitating rubble asteroids. *BAAS* **39**, 50.07.

Burns, J. A., D. P. Simonelli, M. R. Showalter, D. P. Hamilton, C. C. Porco, L. W. Esposito, and H. Throop 2004. Jupiter's ring-moon system. In F. Bagenal and T. Dowling (Eds.), *Jupiter. The Planet, Satellites and Magnetosphere*, pp. 241–262. Cambridge, UK: Cambridge U. Press.

Chandrasekhar, S. 1969. *Ellipsoidal Figures of Equilibrium.* New Haven, CT: Yale Univ. Press.

Chen, W. F., and D. J. Han 1988. *Plasticity for Structural Engineers.* New York: Springer-Verlag.

Cooper, N. J., C. D. Murray, M. W. Evans, K. Beurle, R. A. Jacobson, and C. C. Porco 2008. Astrometry and dynamics of Anthe (S/2007 S 4), a new satellite of Saturn. *Icarus* **195**, 765–777.

Cooper, N. J., C. D. Murray, C. C. Porco, and J. N. Spitale 2006. Cassini ISS astrometric observations of the inner Jovian satellites, Amalthea and Thebe. *Icarus* **181**, 223–234.

Darwin, G. 1906. On the figure and stability of a liquid satellite. *Phil. Trans. R Soc. A* **206**, 161–248.

Davidsson, B. 1999. Tidal splitting and rotational breakup of solid spheres. *Icarus* **142**, 525–535.

Davidsson, B. 2001. Tidal splitting and rotational breakup of solid biaxial ellipsoids. *Icarus* **149**, 375–383.

Dobrovolskis, A. R. 1982. Internal stresses in Phobos and other triaxial bodies. *Icarus* **52**, 136–148.

Dobrovolskis, A. R. 1990. Tidal disruption of solid bodies. *Icarus* **88**, 24–38.

Duxbury, T. C., and J. D. Callahan 1989. Phobos and Deimos control networks. *Icarus* **77**, 275–286.

Fung, Y. C. 1965. *Foundations of Solid Mechanics*. Englewood Cliffs, NJ: Prentice-Hall.

Greenwood, D. T. 1988. *Principles of Dynamics*. Englewood Cliffs, NJ: Prentice-Hall.

Holsapple, K. A. 2001. Equilibrium configurations of solid cohesionless bodies. *Icarus* **154**, 432–448.

Holsapple, K. A. 2008. Spinning rods, elliptical disks and solid ellipsoidal bodies: Elastic and plastic stresses and limit spins. *Int. J. Non-Linear Mech.*, doi:10.1016/j.ijnonlinmec.2008.03.011.

Holsapple, K. A., and P. Michel 2006. Tidal disruptions: A continuum theory for solid bodies. *Icarus* **183**, 331–348.

Holsapple, K. A., and P. Michel 2008. Tidal disruptions II. A continuum theory for solid bodies with strength with applications to the Solar System. *Icarus* **193**, 283–301.

Jacobson, R. A. 1998. The orbits of the inner Uranian satellites from Hubble space telescope and Voyager 2 observations. *AJ* **115**, 1195–1199.

Jacobson, R. A., and W. M. Owen, Jr. 2004. The orbits of the inner Neptunian satellites from Voyager, Earth-based, and Hubble Space Telescope observations. *AJ* **128**, 1412–1417.

Jacobson, R. A., J. Spitale, C. C. Porco, K. Beurle, N. J. Cooper, M. W. Evans, and C. D. Murray 2008. Revised orbits of Saturn's small inner satellites. *AJ* **135**, 261–263.

Karkoschka, E. 2001. Voyager's eleventh discovery of a satellite of Uranus and photometry and the first size measurements of nine satellites. *Icarus* **151**, 69–77.

Karkoschka, E. 2003. Sizes, shapes, and albedos of the inner satellites of Neptune. *Icarus* **162**, 400–407.

Kinoshita, H. 1972. First-order perturbations of the two finite body problem. *Publ. Astron. Soc. Japan* **24**, 423–457.

Knowles, J. K. 1998. *Linear Vector Spaces and Cartesian Tensors*. Oxford: Oxford U. Press.

Love, A. E. H. 1946. *A Treatise on the Mathematical Theory of Elasticity* (4th ed.). New York: Dover.

Murray, C. D., and S. F. Dermott 1999. *Solar System Dynamics*. Cambridge:

Cambridge U. Press.
Nedderman, R. M. 1992. *Statics and Kinematics of Granular Materials*. Cambridge: Cambridge U. Press.
Porco, C. C. 1991. An explanation of Neptune's ring arcs. *Science* **400**, 995–1001.
Porco, C. C., and 35 others 2005. Cassini imaging science: Initial results on Saturn's rings and small satellites. *Science* **307**, 1226–1236.
Porco, C. C., P. C. Thomas, J. W. Weiss, and D. C. Richardson 2007. Saturn's small inner moons: Clues to their origins. *Science* **318**, 1602–1607.
Porco, C. C., J. W. Weiss, P. C. Thomas, D. C. Richardson, R. A. Jacobson, and J. Spitale 2006. Physical characteristics and possible accretionary origins for Saturn's small satellites. In S. Mackwell and E. Stansbery (Eds.), *37th Annual Lunar and Planetary Science Conference*, Volume 37 of *Lunar and Planetary Institute Conference Abstracts*, pp. 2289–2289.
Richardson, D. C., P. Elankumaran, and R. E. Sanderson 2005. Numerical experiments with rubble piles: Equilibrium shapes and spins. *Icarus* **173**, 349–361.
Roche, E. 1847. La figure d'une masse fluide soumise á l'attraction d'un point éloigné. *Acad. des Sci. de Montpellier* **1**, 243–262.
Schaeffer, D. G. 1987. Instability in the evolution equations describing incompressible granular flow. *J. Diff. Equations* **66**, 19–50.
Scheeres, D. J. 2006. Relative equilibria for general gravity fields in the sphere-restricted full 2-body problem. *Celest. Mech. Dyn. Astr.* **94**, 317–349.
Sharma, I. 2004. *Rotational Dynamics of Deformable Ellipsoids with Applications to Asteroids*. Ph. D. thesis, Cornell University.
Sharma, I., J. T. Jenkins, and J. A. Burns 2005a. Equilibrium configurations and the Roche limit for spinning ellipsoidal soil-like asteroids. *BAAS* **37**, 643.
Sharma, I., J. T. Jenkins, and J. A. Burns 2005b. Equilibrium shapes of ellipsoidal soil asteroids. In R. García-Rojo, H. J. Hermann, and S. McNamara (Eds.), *Proceedings of the 5th International Conference on Micromechanics of Granular Media*, Volume 1, pp. 429–432. A. A. Balkema.
Sharma, I., J. T. Jenkins, and J. A. Burns 2006. Tidal encounters of ellipsoidal granular asteroids with planets. *Icarus* **183**, 312–330.
Sharma, I., J. T. Jenkins, and J. A. Burns 2008. Dynamical passage to approximate equilibrium shapes for spinning, gravitating rubble asteroids. *Icarus*, In review.
Shor, V. A. 1975. The motion of the Martian satellites. *Celest. Mech. Dyn. Astr.* **12**, 61–75.
Showalter, M. R., and J. J. Lissauer 2006. The second ring-moon system of Uranus: Discovery and dynamics. *Science* **311**, 973–977.
Thomas, P. C., J. A. Burns, L. Rossier, D. Simonelli, J. Veverka, C. R. Chapman, K. Klaasen, T. V. Johnson, and M. J. S. Belton 1998. The small inner satellites of Jupiter. *Icarus* **135**, 360–371.
Thomas, P. C., C. Weitz, and J. Veverka 1989. Small satellites of Uranus:

Disk-integrated photometry and estimated radii. *Icarus* **81**, 92–101.

Truesdell, C., and R. A. Toupin 1960. The classical field theories. In S. Flügge (Ed.), *Encyclopedia of Physics Vol. III/I: Principles of classical mechanics and field theory*, pp. 226–793. Berlin: Springer-Verlag.

Werner, R. A., and D. J. Scheeres 2005. Mutual potential of homogeneous polyhedra. *Celest. Mech. Dyn. Astr.* **91**, 337–349.

## A Cartesian tensors and coordinate systems

In this paper, we will need to employ two separate cartesian coordinate systems, viz., the principal-axes coordinate systems attached to the primary and the satellite that are defined by the unit vectors $\hat{\mathsf{e}}'_i$ and $\hat{\mathsf{e}}_i$, respectively. These two coordinate systems are shown in Fig. 1, where they are denoted by $P$ and $S$. The components of a vector $\mathsf{a}$ in $P$ will be denoted by $a'_i$ and in $S$ by $a_i$, so that we have the identities

$$\mathsf{a} = (\mathsf{a}\cdot\hat{\mathsf{e}}'_i)\hat{\mathsf{e}}'_i = a'_i\hat{\mathsf{e}}'_i = (\mathsf{a}\cdot\hat{\mathsf{e}}_i)\hat{\mathsf{e}}_i = a_i\hat{\mathsf{e}}_i, \tag{A.1}$$

where we have, and subsequently will employ, indical notation.

Because of the several possible relative orientations of $P$ and $S$, we seek to develop a coordinate-free representation. To this end, we utilize a tensor-based approach. A first-order tensor is simply a vector. A second-order tensor, say $\boldsymbol{A}$, is the coordinate-independent counterpart of a matrix, so that $\boldsymbol{A}$ also operates on a vector to produce another vector. Third- and fourth-order tensors relating lower-order tensors to other lower-order tensors may be similarly defined.

To better understand tensors, it is useful to generalize the concept of a unit vector to a tensorial basis. Such a generalization is furnished by the tensor product $(\mathsf{a}\otimes\mathsf{b})$ of two vectors $\mathsf{a}$ and $\mathsf{b}$. The entity $\mathsf{a}\otimes\mathsf{b}$ is a second-order tensor that can act on another vector $\mathsf{c}$ in two different ways to yield another vector:

$$(\mathsf{a}\otimes\mathsf{b})\cdot\mathsf{c} = (\mathsf{c}\cdot\mathsf{b})\mathsf{a} \quad \text{and} \quad \mathsf{c}\cdot(\mathsf{a}\otimes\mathsf{b}) = (\mathsf{c}\cdot\mathsf{a})\mathsf{b}\,, \tag{A.2}$$

where the '.' on the left hand sides denotes a tensor operation, and the usual vector dot product on the right hand sides. The computation,

$$\mathsf{a}\otimes\mathsf{b} = a_i\hat{\mathsf{e}}_i\otimes b_j\hat{\mathsf{e}}_j = (a_ib_j)\hat{\mathsf{e}}_i\otimes\hat{\mathsf{e}}_j \Longleftrightarrow a'_i\hat{\mathsf{e}}'_i\otimes b'_j\hat{\mathsf{e}}'_j = (a'_ib'_j)\hat{\mathsf{e}}'_i\otimes\hat{\mathsf{e}}'_j, \tag{A.3}$$

suggests that a tensorial basis may be constructed by taking appropriate order tensor products of the unit vectors. Thus, a second-order tensorial basis in the primary's coordinate system $P$ is given by the nine quantities $\hat{\mathsf{e}}'_i\otimes\hat{\mathsf{e}}'_j$. Similarly we have $\hat{\mathsf{e}}_i\otimes\hat{\mathsf{e}}_j$ in $S$. A second-order tensor $\boldsymbol{A}$ can then be written as

$$\boldsymbol{A} = A'_{ij}\hat{\mathsf{e}}'_i\otimes\hat{\mathsf{e}}'_j = A_{ij}\hat{\mathsf{e}}_i\otimes\hat{\mathsf{e}}_j, \tag{A.4}$$

in terms of $\boldsymbol{A}$'s components $A_{ij}$ in $P$ and $A'_{ij}$ in $S$, respectively. These components, obtained by appealing to (A.2), are given by the equations

$$A'_{ij} = \hat{\mathsf{e}}'_i \cdot \boldsymbol{A} \cdot \hat{\mathsf{e}}'_j \quad \text{and} \quad A_{ij} = \hat{\mathsf{e}}_i \cdot \boldsymbol{A} \cdot \hat{\mathsf{e}}_j, \tag{A.5}$$

that are reminiscent of analogous ones for vector components; see (A.1). We will refer to the nine $A_{ij}$'s ($A'_{ij}$) as the "*matrix* of $\boldsymbol{A}$ in $S$ ($P$)" denoted by $[\boldsymbol{A}]$ ($[\boldsymbol{A}]'$). A second-order tensor's interactions with vectors and other second-order tensors may be obtained by repeated (if required) application of (A.2). These operations are summarized below:

$$\boldsymbol{A} \cdot \mathsf{a} = A_{ij}\hat{\mathsf{e}}_i \otimes \hat{\mathsf{e}}_j \cdot a_m \hat{\mathsf{e}}_m = A_{ij}a_j\hat{\mathsf{e}}_i \tag{A.6a}$$

$$\mathsf{a} \cdot \boldsymbol{A} = a_m\hat{\mathsf{e}}_m \cdot A_{ij}\hat{\mathsf{e}}_i \otimes \hat{\mathsf{e}}_j = a_i A_{ij}\hat{\mathsf{e}}_j, \tag{A.6b}$$

$$\boldsymbol{A} \cdot \boldsymbol{B} = A_{ij}\hat{\mathsf{e}}_i \otimes \hat{\mathsf{e}}_j \cdot B_{mn}\hat{\mathsf{e}}_m \otimes \hat{\mathsf{e}}_n = A_{ij}B_{jn}\hat{\mathsf{e}}_i \otimes \hat{\mathsf{e}}_n \tag{A.6c}$$

$$\text{and} \quad \boldsymbol{A} : \boldsymbol{B} = A_{ij}\hat{\mathsf{e}}_i \otimes \hat{\mathsf{e}}_j : B_{mn}\hat{\mathsf{e}}_m \otimes \hat{\mathsf{e}}_n = A_{ij}\hat{\mathsf{e}}_i \cdot B_{jn}\hat{\mathsf{e}}_n = A_{ij}B_{ji}, \tag{A.6d}$$

where the first two operations produce vectors, the next another second-order tensor, and the third a scalar. The double-dot product (:), as its form suggests, denotes a sequential application of dot products. $\boldsymbol{A}$'s actions on higher-order tensors may be analogously defined. When there is no confusion, second-order tensors are referred to simply as tensors.

The transpose ('T') and inverse ('-1') of a tensor $\boldsymbol{A}$ may be interpreted from their corresponding matrix definitions

$$[\boldsymbol{A}^T] = [\boldsymbol{A}]^T \quad \text{and} \quad [\boldsymbol{A}^{-1}] = [\boldsymbol{A}]^{-1}. \tag{A.7}$$

If $\boldsymbol{S}$ is a symmetric tensor, i.e., $\boldsymbol{S}^T = \boldsymbol{S}$, it is possible to find an orthogonal coordinate system, say the $\hat{\mathsf{e}}'_i$ of $P$, in which $\boldsymbol{S}$'s matrix is diagonal, so that we may write

$$\boldsymbol{S} = \sum_{i=1}^{3} S'_i \hat{\mathsf{e}}'_i \otimes \hat{\mathsf{e}}'_i, \tag{A.8}$$

where $S'_i$, the components of $\boldsymbol{S}$ in $P$ are called the eigenvalues of $\boldsymbol{S}$ corresponding to $\boldsymbol{S}$'s eigenvectors $\hat{\mathsf{e}}'_i$. Finally, to every vector $\mathsf{w}$, there corresponds an anti-symmetric tensor $\boldsymbol{W} = -\boldsymbol{W}^T$ that is formed by the components of $\mathsf{w}$ in any coordinate system, i.e.,

$$\boldsymbol{W} = -\varepsilon_{ijk} w'_i \hat{\mathsf{e}}'_j \otimes \hat{\mathsf{e}}'_k = -\varepsilon_{ijk} w_i \hat{\mathsf{e}}_j \otimes \hat{\mathsf{e}}_k, \tag{A.9}$$

where $\varepsilon_{ijk}$ is the alternating third-order tensor (see below), such that $\varepsilon_{ijk} = 1$ or -1, if $i \neq j \neq k$ form an even or an odd permutation, respectively, and 0 otherwise.

In the sequel, we will need to find the components of vectors and second-order tensors in one coordinate system, say $S$, given its matrix in the other, say $P$.

This may be done by expressing the unit vectors of $P$ in terms of those of $S$ as,

$$\hat{\mathsf{e}}'_i = (\hat{\mathsf{e}}'_i \cdot \hat{\mathsf{e}}_j)\hat{\mathsf{e}}_j,$$

and substituting this relationship into the first of (A.1) and (A.5). Geometrically, because both $P$ and $S$ are right-handed Cartesian coordinate systems, it is possible to obtain one from the other by a rotation. A rotation, because it takes vectors to vectors, is a second-order tensor, and we write

$$\hat{\mathsf{e}}'_i = \boldsymbol{T} \cdot \hat{\mathsf{e}}_i,$$

in terms of the rotation tensor $\boldsymbol{T} = T'_{ij}\hat{\mathsf{e}}'_i \otimes \hat{\mathsf{e}}'_j = T_{ij}\hat{\mathsf{e}}_i \otimes \hat{\mathsf{e}}_j$. It may be shown that, in fact,

$$T_{ij} = [\boldsymbol{T}]_{ij} = T'_{ij} = [\boldsymbol{T}]'_{ij} \equiv \hat{\mathsf{e}}'_j \cdot \hat{\mathsf{e}}_i. \tag{A.10}$$

Substituting the previous two equations into (A.1) and (A.5), we obtain the coordinate transformation rules

$$[\mathsf{a}] = [\boldsymbol{T}^T \cdot \mathsf{a}]' = [\boldsymbol{T}]^T[\mathsf{a}]' \Longleftrightarrow a_i = T_{ji}a'_j \tag{A.11a}$$

$$\text{and} \quad [\boldsymbol{A}] = [\boldsymbol{T}^T \cdot \boldsymbol{A} \cdot \boldsymbol{T}]' = [\boldsymbol{T}]^T[\boldsymbol{A}]'[\boldsymbol{T}] \Longleftrightarrow A_{ij} = T_{ki}A'_{kl}T_{lj} \tag{A.11b}$$

for vector and second-order tensor components, respectively.

Next, consider third-order tensors. In terms of the third-order tensorial bases, $\hat{\mathsf{e}}'_i \otimes \hat{\mathsf{e}}'_j \otimes \hat{\mathsf{e}}'_k$ in $P$ and $\hat{\mathsf{e}}_i \otimes \hat{\mathsf{e}}_j \otimes \hat{\mathsf{e}}_k$ in $S$, a third-order tensor is defined as

$$\boldsymbol{\mathcal{A}} = A'_{ijk}\hat{\mathsf{e}}'_i \otimes \hat{\mathsf{e}}'_j \otimes \hat{\mathsf{e}}'_k = A_{ijk}\hat{\mathsf{e}}_i \otimes \hat{\mathsf{e}}_j \otimes \hat{\mathsf{e}}_k, \tag{A.12}$$

so that $A'_{ijk}$ and $A_{ijk}$ are the components in $P$ and $S$, respectively. The actions of $\boldsymbol{\mathcal{A}}$ on vectors and other tensors of various orders are defined in a manner similar to that of a second-order tensor (A.6), e.g.,

$$\boldsymbol{\mathcal{A}} \cdot \mathsf{a} = A_{ijk}\hat{\mathsf{e}}_i \otimes \hat{\mathsf{e}}_j \otimes \hat{\mathsf{e}}_k \cdot a_m\hat{\mathsf{e}}_m = A_{ijk}a_k\hat{\mathsf{e}}_i \otimes \hat{\mathsf{e}}_j \tag{A.13a}$$

$$\text{and} \quad \mathsf{a} \cdot \boldsymbol{\mathcal{A}} = a_m\hat{\mathsf{e}}_m \cdot A_{ijk}\hat{\mathsf{e}}_i \otimes \hat{\mathsf{e}}_j \otimes \hat{\mathsf{e}}_k = a_iA_{ijk}\hat{\mathsf{e}}_j \otimes \hat{\mathsf{e}}_k. \tag{A.13b}$$

Fourth-order tensors are formed in a manner analogous to third-order tensors,

$$\mathsf{A} = A'_{ijkl}\hat{\mathsf{e}}'_i \otimes \hat{\mathsf{e}}'_j \otimes \hat{\mathsf{e}}'_k \otimes \hat{\mathsf{e}}'_l = A_{ijkl}\hat{\mathsf{e}}_i \otimes \hat{\mathsf{e}}_j \otimes \hat{\mathsf{e}}_k \otimes \hat{\mathsf{e}}_l, \tag{A.14}$$

and their operations on vectors and tensors of various orders may be developed by following (A.6) and (A.13), for example,

$$\mathsf{A} : \boldsymbol{B} = A_{ijkl}\hat{\mathsf{e}}_i \otimes \hat{\mathsf{e}}_j \otimes \hat{\mathsf{e}}_k \otimes \hat{\mathsf{e}}_l : B_{mn}\hat{\mathsf{e}}_m \otimes \hat{\mathsf{e}}_n = A_{ijkl}B_{lk}\hat{\mathsf{e}}_i \otimes \hat{\mathsf{e}}_j. \tag{A.15}$$